HHS Public Access

Author manuscript

Cell. Author manuscript; available in PMC 2024 December 14.

Published in final edited form as:

Cell. 2024 December 12; 187(25): 7091–7106.e24. doi:10.1016/j.cell.2024.10.020.

STK19 positions TFIIH for cell-free transcription-coupled DNA repair

Tycho E.T. Mevissen[1,3], **Maximilian Kümmecke**[2], **Ernst W. Schmid**[1], **Lucas Farnung**[2,*], **Johannes C. Walter**[1,3,4,*]

[1]Department of Biological Chemistry and Molecular Pharmacology, Blavatnik Institute Harvard Medical School, Boston, MA 02115, USA

[2]Department of Cell Biology, Blavatnik Institute, Harvard Medical School, Boston, MA 02115, USA

[3]Howard Hughes Medical Institute

[4]Lead contact

SUMMARY

In transcription-coupled repair, stalled RNA polymerase II (Pol II) binds CSB and CRL4^{CSA}, which cooperate with UVSSA and ELOF1 to recruit TFIIH for nucleotide excision repair (TC-NER). To explore the mechanism of TC-NER, we recapitulated this reaction *in vitro*. When a plasmid containing a site-specific lesion is transcribed in frog egg extract, error-free repair is observed that depends on CSB, CRL4^{CSA}, UVSSA, and ELOF1. Repair also requires STK19, a factor previously implicated in transcription recovery after UV exposure. A 1.9 Å cryo-electron microscopy structure shows that STK19 binds the TC-NER complex through CSA and the RPB1 subunit of Pol II. Furthermore, AlphaFold predicts that STK19 interacts with the XPD subunit of TFIIH, and disrupting this interface impairs cell-free repair. Molecular modeling suggests that STK19 positions TFIIH ahead of Pol II for lesion verification. Our analysis of cell-free TC-NER suggests that STK19 couples RNA polymerase II stalling to downstream repair events.

In Brief

*Correspondence: johannes_walter@hms.harvard.edu, lucas_farnung@hms.harvard.edu.

AUTHOR CONTRIBUTIONS

J.C.W and T.E.T.M. conceived and T.E.T.M. performed and analyzed all experiments except for cryo-EM studies. T.E.T.M carried out structure predictions, and SPOC analysis was performed by E.W.S. Cryo-EM protein preparation, complex formation, and cryo-EM analysis were conceived and performed by M.K. and L.F. The atomic model was built by L.F. The manuscript was written by T.E.T.M and J.C.W., with help from L.F.

DECLARATION OF INTERESTS

J.C.W. is a co-founder of MOMA therapeutics, in which he has a financial interest.

Together with structural analyses, a cell-free system for transcription-coupled nucleotide excision repair (TC-NER) shows that STK19 is an integral component of the TC-NER complex that couples RNA polymerase II stalling to downstream repair events.

Graphical Abstract

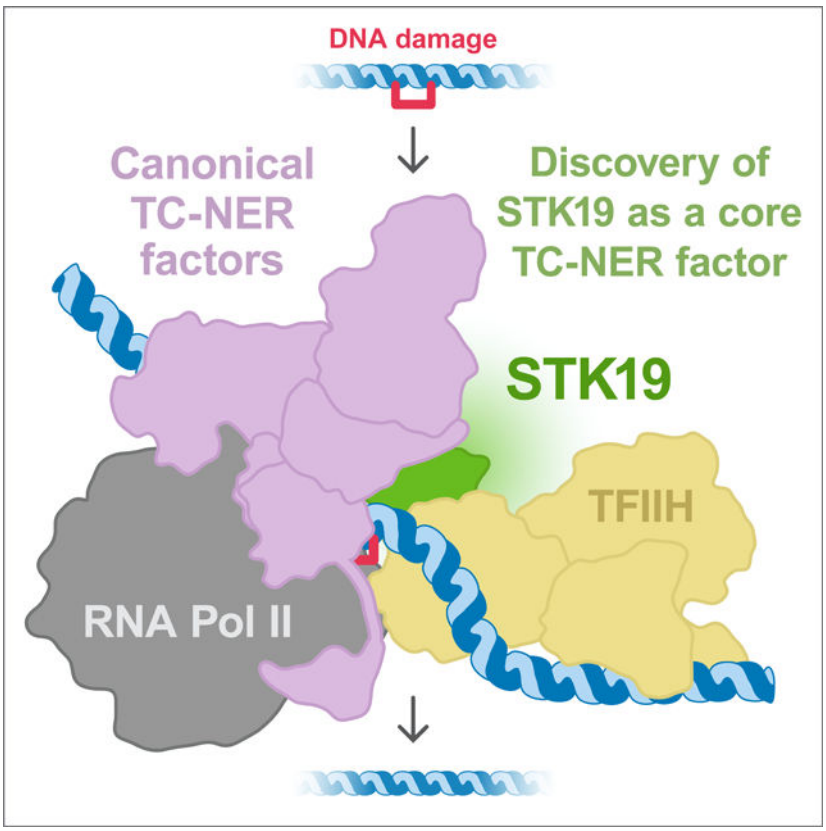

INTRODUCTION

Our cells contain numerous mechanisms to repair DNA damage that is continually generated by diverse endogenous and exogenous agents. A particularly versatile pathway is nucleotide excision repair (NER), which removes bulky DNA adducts regardless of their chemical structure.[1–5] In global genome (GG)-NER, which can in principle operate at any locus, Xeroderma pigmentosum group protein C (XPC) in complex with RAD23B and Centrin 2 (CETN2) recognizes the distortion in DNA structure created by bulky lesions. This heterotrimeric complex then recruits TFIIH, whose XPB ATPase subunit unwinds DNA surrounding the lesion, and whose XPD ATPase subunit searches one strand for the presence of DNA damage.[6] If a lesion is detected, TFIIH recruits the downstream repair machinery, including two structure-specific endonucleases, XPF-ERCC1 and XPG, which incise the damaged strand on either side of the lesion. The damaged oligonucleotide dissociates from DNA, and gap filling completes the repair reaction. GG-NER has been reconstituted with purified components and is therefore relatively well-understood.[1,7,8]

Almost 40 years ago, the Hanawalt group discovered that DNA damage located in the transcribed strand of a gene is preferentially repaired by NER, leading to the concept of transcription-coupled (TC)-NER.[9–11] In this mechanism, DNA damage is sensed by RNA polymerase II (Pol II) stalling instead of by XPC-RAD23B-CETN2. Four factors have been identified that couple Pol II stalling to TFIIH recruitment and the downstream repair steps that operate in GG-NER.[12] The first is CSB, which is mutated in a human neurodegenerative progeroid syndrome called Cockayne syndrome. CSB is a SWI/SNF-type ATPase that binds on the upstream side of stalled Pol II and attempts to push it past obstacles.[13,14] If the obstacle is insurmountable, as seen for many DNA lesions, CSB recruits the $CRL4^{CSA}$ E3 ubiquitin ligase whose substrate receptor CSA links to a CUL4 scaffold via DDB1. CSB recruits $CRL4^{CSA}$ via a short CSA-interacting motif (CIM) that binds directly to CSA.[15] $CRL4^{CSA}$ transfers ubiquitin to lysine 1268 of RPB1, the largest subunit of Pol II,[16] and this modification helps recruit TFIIH via an unknown mechanism. The third TC-NER factor that is also a transcription elongation factor, ELOF1, interacts with Pol II and $CRL4^{CSA}$, and it is required for efficient Pol II polyubiquitination.[17–19] Finally, UV-stimulated scaffold protein A (UVSSA),[20–22] is recruited to stalled Pol II via a direct interaction with CSA,[14] and UVSSA binding and Pol II ubiquitination appear to be interdependent.[16] In turn, UVSSA interacts with and is essential to recruit TFIIH to the repair complex via direct binding to the p62 subunit.[15,23,24] However, TFIIH interacts with an unstructured region of UVSSA (the TFIIH-interacting region, TIR), leaving open the question of how TFIIH is properly positioned ahead of Pol II to recognize the damaged strand. Thus, the coupling mechanism between stalled Pol II and repair remains incompletely understood.

Serine threonine kinase 19 (STK19) was nominated by several groups as a possible TC-NER factor.[17,25–27] Despite its name, STK19 bears no resemblance to protein kinases, and the purified protein has no detectable kinase activity.[27,28] Recent reports demonstrated that STK19 interacts with DNA and that mutations identified in cancer patients impair DNA binding.[27,29] STK19 confers resistance to the alkylating agent illudin S, as seen for other TC-NER factors,[17,26] and it promotes transcription recovery after UV exposure.[25] These observations are consistent with a role for STK19 in TC-NER but might also indicate a specific function in transcription restart. Thus, whether STK19 is a core TC-NER factor and what role it plays in the response to DNA damage are unanswered questions.

A full understanding of TC-NER requires biochemical and structural analysis. A prior study showed that CSB and GG-NER factors promote a low level of repair from a lesion-stalled Pol II.[30] However, the recruitment of TFIIH to the lesion was CSB-independent, and the reaction presumably did not contain $CRL4^{CSA}$, UVSSA, or ELOF1. More recently, RNA polymerase II complexes containing CSB, $CRL4^{CSA}$, UVSSA, and ELOF1 have been determined by cryo-EM.[14,19,31] However, the transition to downstream repair events has not been structurally resolved. Thus, a full mechanistic understanding of TC-NER is still lacking.

Given that *X. laevis* egg extracts recapitulate numerous DNA repair pathways including GG-NER,[32,33] we asked whether they might also support TC-NER. To this end, we first recapitulated efficient and inducible *in vitro* transcription in egg extracts using a plasmid with a strong promoter. Placement of a cisplatin intrastrand crosslink in the template strand

downstream of the promoter led to Pol II stalling but no TC-NER. When we supplemented the extract with recombinant CSB, $CRL4^{CSA}$, UVSSA, ELOF1, and STK19, we observed lesion repair that was independent of XPC and abolished by the Pol II inhibitor α-amanitin. Repair required all five of the above factors, demonstrating *bona fide* TC-NER *in vitro* and indicating that STK19 is an essential TC-NER factor. To understand how STK19 promotes repair, we used AlphaFold-Multimer and single-particle cryo-EM to elucidate its interaction with the TC-NER machinery. Together with structure-function analyses, we find that STK19 is an integral component of the TC-NER complex that interacts with $CRL4^{CSA}$ and RPB1. Molecular modeling and site-directed mutagenesis further suggests that STK19 positions TFIIH in front of the TC-NER complex for lesion verification by the XPD helicase. Our work suggests that STK19 forms the linchpin between lesion-stalled Pol II and downstream repair events.

RESULTS

Inducible transcription in frog egg extracts

To recapitulate cell-free TC-NER, we first sought to achieve efficient and inducible transcription in frog egg extracts. To this end, we constructed a plasmid containing a strong basal promoter flanked by GAL4 upstream activating sequences (UAS; Figure 1A). The plasmid was added to a concentrated nucleoplasmic extract (NPE) derived from frog eggs that was also supplemented with TBP, the transcriptional activator GAL4-VP64, and radioactive UTP (Figure 1A). Unlike a total egg lysate, NPE supported transcription (Figure S1A, lanes 1–3 and 7–9) that was greatly stimulated by GAL4-VP64 and TBP (Figure S1A, lanes 10–12). Transcription efficiency was further enhanced via the use of a synthetic super core promoter (Figure S1B) and molecular crowding agents (Figure S1C). When we combined all the above features, transcription greatly exceeded the level observed from an endogenous promoter in NPE (Figure S1D).[34] Other properties of this inducible, cell-free transcription system will be described elsewhere.

Cell-free TC-NER in egg extract

Having achieved efficient cell-free transcription, we sought to recapitulate TC-NER *in vitro*. To this end, we placed a cisplatin 1,3-GTG intrastrand crosslink in the transcribed DNA strand 122 or 322 base pairs downstream of the transcription start site (Figure 1A). These lesions induced a potent block to transcription at the expected location (Figure 1B, lanes 4–6 and 10–12). To measure repair, we asked whether a *PmlI* restriction site that coincides with the crosslink is regenerated (Figure 1A). As shown in Figure 1C, the *PmlI* site was regenerated in NPE regardless of whether transcription was induced (lanes 2–7), and repair was unaffected by the transcription inhibitor α-amanitin (lanes 8–10; Figure S1E). When we inhibited or depleted the GG-NER factor XPC, repair was greatly reduced (Figure S1F). Thus, naïve NPE only supported GG-NER, even in the presence of transcription.

Based on mass spectrometry analysis, egg extracts contain low or undetectable levels of CSB, CSA, UVSSA, ELOF1, and the candidate TC-NER factor, STK19.[35] Furthermore, western blotting indicated that the concentrations of CSB and CSA are low in the egg and increase during development (Figure S2A). Based on these observations, we hypothesized

that the absence of TC-NER in NPE was due to the absence of one or more TC-NER factors in this extract. To test this idea, we expressed recombinant CSB, CRL4^{CSA}, ELOF1, UVSSA, and STK19 (all proteins are from *X. laevis* except CSB, which is human; see Figure S2B and its legend), and combined them to make a "TC-NER cocktail." Strikingly, in extracts that were undergoing transcription and where XPC-dependent GG-NER was inhibited, the addition of this cocktail stimulated repair (Figure 1D, compare conditions II and III; Figures 1E and 1F for quantification). Moreover, repair was returned to basal levels by the addition of α-amanitin (condition IV). Importantly, this repair was strand specific because a crosslink in the non-template strand did not stall Pol II (Figure S1G) or undergo repair in the presence of the TC-NER cocktail (Figure S1H), whereas GG-NER repaired lesions in either strand (Figure S1I). The induction of XPC-independent repair of a template strand crosslink that requires transcription and a cocktail of TC-NER factors strongly suggested that NPE can support cell-free TC-NER.

Cell-free repair requires all canonical TC-NER factors, as well as STK19

To further test whether our cell-free system recapitulates *bona fide* TC-NER, we omitted each of the five proteins from the cocktail. When CSB was omitted, TC-NER was abolished, but CSB alone supported little repair (Figure 2A, conditions II-IV; Figure S2C). Therefore, CSB is necessary but not sufficient to induce TC-NER in NPE. In the absence of each of the other four factors, repair was modestly reduced (Figure 2A, conditions V-VIII; Figures S2D-S2G). This finding suggested that these four factors are individually not required for cell-free TC-NER, or that the endogenous proteins are sufficient to support repair, despite being undetectable in some cases. To distinguish between these possibilities, we depleted each protein from the extract. When CSA was depleted from NPE and omitted from the cocktail, repair was dramatically reduced, and it was restored by the inclusion of CRL4^{CSA} or CSA-DDB1 in the cocktail (see Methods) (Figure 2B, conditions III and IV; Figure S2D). This result shows that CSA-DDB1 is essential for efficient cell-free TC-NER. Similar results were observed for ELOF1 and UVSSA (Figure 2B, conditions V-VIII; Figures S2E and S2F), demonstrating that cell-free repair in NPE requires all four canonical TC-NER factors (CSB, CRL4^{CSA}, UVSSA, and ELOF1). Finally, STK19 was required, strongly arguing that it is a core TC-NER protein (Figures 2B, conditions IX-X and S2G).

We next addressed whether repair in this system requires previously characterized protein-protein interactions and activities. Repair was inhibited when we disrupted the known interaction between CSA and the CIM of CSB (Figures 2C and S2H), the interactions between ELOF1 and both Pol II and CSA (Figures 2D and S2I), or the interactions between UVSSA and its two binding partners CSA and TFIIH (Figures 2E and S2J).[15,17,19,24] Moreover, repair was blocked by the general cullin inhibitor MLN4924, consistent with CRL4^{CSA} activity being required for TC-NER (Figures 2F and S2K). Finally, using restriction enzymes whose staggered cutting allows differentiation of the two DNA strands (Figure 2G), we verified that cell-free TC-NER involves unscheduled DNA synthesis (UDS) on the damaged template strand (Figure 2H, condition III), as seen for GG-NER (condition I). Altogether, these results show that egg extracts recapitulate all features expected of TC-NER: involvement of CSB, CRL4^{CSA}, ELOF1, and UVSSA; known interactions between these factors; cullin E3 ligase activity; and gap filling on the transcribed strand. Furthermore,

the data provide strong evidence that STK19 is a core TC-NER factor that acts upstream of error-free repair.

Structure of a TC-NER complex containing STK19

To determine how STK19 promotes repair, we used AlphaFold-Multimer (AF-M) to screen for potential STK19 interactors. STK19 was "folded" with 409 proteins involved in genome maintenance and transcription, and each binary structure prediction was assessed using SPOC (Structure Prediction and Omics Classifier), a classifier trained to distinguish functionally relevant from spurious AF-M complexes of human proteins (0–1 scale; >0.5 is a strong candidate for a meaningful interaction).[36] Among the proteins examined, RPB1 (Pol II subunit 1), XPD (ERCC2), and CSA (ERCC8) were the top hits (Figure 3A; see Figures S3A and S3B for conventional confidence metrics; Table S1). By folding CSB, CSA, DDB1, DDA1 (a component of CRL4 E3 ligases),[37] ELOF1, UVSSA, and STK19 all at once, we generated a structure prediction for an STK19-containing TC-NER complex (Figures 3B and 3C; but lacking Pol II) that allowed us to initiate structure-function analyses of STK19 and other TC-NER proteins (see below).

We subsequently used single-particle cryo-EM to solve the structure of STK19 bound to a Pol II elongation complex containing CSB, CSA-DDB1, DDA1, ELOF1, and UVSSA (Figure S4). We collected and analyzed a cryo-EM dataset (Figures S5 and S6) and obtained a structure at an overall resolution of 1.9 Å from 484,012 particles (Figure 3D). In our structure, Pol II adopts a post-translocated state, and we resolve water molecules that coordinate the metal A in the active site (Figure 3E). CSB embraces the upstream DNA, and its ATPase motor is in a pre-translocated state.[14] The atomic model of the TC-NER complex was real-space refined and shows excellent stereochemistry (Tables S2 and S3). High-resolution features allowed us to unambiguously place a structure of the RNA polymerase II-TC-NER complex with ELOF1 into our density.[19] We also observed well-resolved features for STK19, allowing us to unambiguously dock an AlphaFold model of STK19 into the corresponding density, which showed that STK19 binds the TC-NER complex primarily via RPB1 and an extensive interface with CSA (Figure 3D; see below for a detailed description), as predicted by AF-M (Figure 3B). Additional density corresponding to DDA1 on DDB1 could be built using an AF-M prediction. DDA1 interacts with DDB1 as observed before (Figure 3F).[38]

Our TC-NER complex also contained additional densities, leading to a more complete model of this assembly. First, we modeled additional N- and C-terminal parts of CSB that bind intramolecularly to CSB ATPase lobes 1 and 2, respectively (Figure 3G). Second, besides the known interaction of CSA with the CIM of CSB,[14,15] we also observed an adjacent contact between highly conserved CSB residues 1329–1336 and CSA, which we name CSA-interacting peptide (CIP) (Figures 3G and S3C). Specifically, CSB R1330 contacts CSA Y58, F1331 of CSB inserts into a cavity formed between WD40 repeats 1 and 2 of CSA, and CSB K1334 forms a salt bridge with E55 of CSA. Third, we extended the model for the linker region between the UVSSA zinc finger domain and the UVSSA C-terminus and completed the DDB1 model by resolving additional residues in the previously unobserved flexible loops. Fourth, the previously unresolved C-terminal tail of CSA was

seen to interact with DDB1 and the VHS domain of UVSSA (Figure 3D; described in more detail below). Lastly, we resolved and modeled an additional loop of the RPB1 jaw (residues 1261–1281) containing K1268, which is ubiquitinated during TC-NER.[16,39] Our structure shows that the loop is positioned above the UVSSA C-terminus, with UVSSA residue R669 inserting into the cavity formed by the RPB1 jaw and the K1268 loop (Figures 3D and 3H). Remarkably, almost all of the above features were correctly predicted by AF-M (Figure 3B; Figures S3D and S3E; see below).

The interaction of STK19 with CSA and DDB1 is required for TC-NER

STK19 comprises three winged helix (WH) domains (Figures 4A and 4B),[27–29] and it contacts the TC-NER complex in four places (Figure 4C). First, STK19 density could be traced from WH1 towards a pocket formed by DDB1 β-propellers A and B (Figure 4D, panel I). Directed by AF-M predictions (Figure 3B), we assigned this additional density to the previously unresolved N-terminus of STK19, which binds to the same DDB1 cavity that is also occupied by the N-terminus of CSA. Second, STK19 residues R72, T73, D76, and R77 in the α3 helix of WH1 contact the linker between CSA WD40 repeats 5 and 6 (Figure 4D, panel II). STK19 destabilizes a CSA loop (residues 231–236) normally seen between WD40 repeats 4 and 5[19] that we could no longer resolve fully. Third, WH2 and the N-terminal part of the WH3 α1 helix directly interact with the RPB1 clamp head (Figure 4D, panel III). Finally, STK19 WH3 inserts into a pocket formed by downstream DNA, UVSSA, and CSA, where K203 in WH3 contacts E10 in UVSSA (Figures 3D and 4D, panel IV). Compared to the previous TC-NER complex with ELOF1,[19] the UVSSA VHS domain is shifted towards the downstream DNA and STK19 by 5–8 Å (Figure 4E). Of note, the interaction between UVSSA and STK19 was not predicted with high confidence (Figure 3A; Figures S3A and S3B), and UVSSA^{E10A} supported efficient TC-NER (Figure 4F), suggesting that the STK19-UVSSA interaction is predominantly facilitated by their common binding partner CSA (Figures 3B and 3D). To further address whether binding of STK19 to the TC-NER complex is important for repair, we deleted the N-terminus of STK19, which projects towards DDB1 (Figure 4D, panel I), resulting in STK19$^{\Delta N}$, or we mutated the four residues at the STK19-CSA interface to alanine (Figure 4D, panel II; *X. laevis* residues in parentheses), yielding STK19^{4A}. Both mutants supported only ~50–60% efficient TC-NER when added to STK19-depleted extract, and combining these mutations lead to a complete loss of repair (Figure 4G). Similarly, reversing two charges at the STK19-CSA interface strongly impaired error-free repair (Figure 4G; STK19$^{DR\text{-}RD}$). We conclude that the interaction of STK19 with the TC-NER complex via interfaces with DDB1 and CSA is essential for STK19 to support cell-free repair.

Mutations at the predicted STK19-XPD interface disrupt TC-NER

While our results show that STK19 binding to CSA and DDB1 is important for TC-NER, they do not explain how this binding promotes repair. Importantly, our *in silico* screen predicted that STK19 also interacts with the XPD subunit of TFIIH via an extensive interface involving STK19's WH3 domain (Figure 5A). This interaction has a high SPOC score in humans (Figure 3A), and it is confidently predicted in other species that have STK19 and XPD, including frogs, fish, plants, and fission yeast (Figure S3F). Based on these structure predictions, we postulated that STK19 positions TFIIH on the TC-NER

complex. Of note, the XPD and UVSSA binding sites on STK19 partly overlap (Figures 5A and 5B), and we provide evidence below suggesting that UVSSA moves to allow formation of the XPD-STK19 complex (Figure 5C and see below). To address the importance of the STK19-XPD interaction, we generated three STK19 mutants that are designed to disrupt three distinct contact points between STK19 and XPD (Figure 5D, panels I-III). These mutations involved changing charged and bulky residues in a loop to two glycines ($STK19^{RY\text{-}GG}$; R209G and Y210G in *X. laevis*), a single charge-swap mutation ($STK19^{D\text{-}R}$; D217R), and replacement of two small side chains in a loop to two larger residues ($STK19^{AS\text{-}EY}$; A250E and S251Y). These mutations reduced TC-NER to various extents, and when all the mutations above were combined, repair was inhibited almost ~4 fold (Figure 5E). Although the $STK19^{RY\text{-}GG}$ mutant also removes a salt bridge with E10 of UVSSA (Figure 4D, panel IV), we showed above that $UVSSA^{E10A}$ is fully proficient for repair. Therefore, the effect of this mutant is likely due to deficient XPD binding. Together, our data suggest that STK19 promotes TC-NER by interacting with XPD.

A model of the TC-NER complex in which STK19 positions XPD on DNA

XPD is the 5’ to 3’ helicase subunit of TFIIH that tracks along the transcribed strand during TC-NER to verify the presence of damage. We asked how the interaction of STK19 with XPD would position TFIIH relative to the TC-NER complex. To this end, we first aligned the STK19-XPD AF-M prediction (Figure 5A) on the cryo-EM structure of the TC-NER complex via STK19 (Figure 5F). Onto the resulting complex, we aligned a previously determined TFIIH-XPA-splayed DNA structure[40] via XPD (Figure 5F). This revealed no major clashes between TFIIH and the TC-NER complex other than the one between XPD and UVSSA mentioned above. In the composite model, STK19 positions TFIIH in front of the TC-NER complex near the downstream DNA, where it searches the template strand for the presence of DNA damage. Strikingly, the 3’ end of the single-stranded DNA emerging from the XPD channel aligns with the 5’ end of the downstream template strand of the TC-NER complex (Figure 5F, right panel, dark blue strands), suggesting that STK19 guides TFIIH to the correct strand for lesion verification. Importantly, in the TC-NER cryo-EM structure, STK19 also contacts downstream DNA (Figure 5D, panel IV), consistent with prior DNA binding studies.[27–29] Specifically, a positively charged surface in the WH3 domain contacts the phosphate backbone. To address the importance of this interaction, we mutated two arginines to alanine (R206A and R207A in *X. laevis*), alone or in combination. The single mutants reduced and the double mutant ($STK19^{RR\text{-}AA}$) strongly impaired DNA binding (Figure 5G). Despite this, all three mutants including $STK19^{RR\text{-}AA}$ had only a minor effect on DNA repair (Figure 5H). In contrast, a mutant in which both charges were reversed ($STK19^{RR\text{-}EE}$) was severely defective in DNA repair. These results suggest that STK19 does not need to attract DNA, but that repelling it is deleterious. Indeed, as shown in Figure 5F (right panel), duplex DNA contacts STK19 immediately adjacent to the place where the template strand enters the XPD channel. Therefore, we propose that STK19 must accommodate DNA in this location to allow template strand entry to the XPD channel.

The C-terminus of CSA interacts with UVSSA

Our model above proposes that STK19 positions TFIIH via XPD binding, yet XPD’s position on STK19 would clash with the VHS domain of UVSSA, which is anchored

nearby via CSA (compare Figures 5C and 6A). Importantly, the VHS domain interacts with CSA in two ways (Figures 6A and 6B, panels I and II): the previously reported interaction with the CSA β-propeller involving Y334 (Figure 6B, panel I) and a second interaction involving the C-terminal tail of CSA (panel II), revealed by AF-M and cryo-EM (Figures 3B and 3D). Several proximal residues in this ~30 amino acid long tail interact with DDB1 (Figure 6B, panel III), and the distal W389 makes a contact with the UVSSA VHS domain (Figure 6B, panel II) that is highly conserved (Figures S7A and S7B). To determine which of these contacts are important to mediate UVSSA-CRL4^{CSA} binding, we measured CRL4^{CSA}-dependent UVSSA ubiquitination *in vitro*. As shown in Figure 6C, mutation of the tryptophan and the adjacent, conserved serine (CSA^{WS-AA}) specifically prevented UVSSA monoubiquitination by CRL4^{CSA} (Figures 6C and S7C). These results indicate that CSA's C-terminus is required to mediate a stable interaction between CRL4^{CSA} and UVSSA. Importantly, these mutations also abolished TC-NER (Figure 6D). In contrast, mutation of the tyrosine that resides at the previously described CSA-UVSSA interface (Figure 6B, panel I) had no effect on UVSSA ubiquitination (Figure 6C; STK19^{Y-A}) or TC-NER (Figure 6D). These results suggest that binding of CSA's flexible C-terminal tail to UVSSA is more important than binding mediated by CSA's β-propeller. We therefore propose that UVSSA can dissociate from the CSA β-propeller to accommodate XPD while remaining tethered to the TC-NER complex via CSA's C-terminal tail (Figure 5C). Together, our results suggest a model that explains how STK19 functionally couples the TC-NER complex to downstream repair events (Figure 7 and see Discussion).

DISCUSSION

We have recapitulated eukaryotic transcription-coupled DNA repair in frog egg extracts, and we use this system to show that STK19 is the missing link between stalled Pol II and TFIIH. We find that extracts depleted of STK19 are deficient for TC-NER, as seen from failure to restore a restriction site at a cisplatin lesion in the template strand. Together with mutational analysis, our 1.9 Å resolution cryo-EM structure of the STK19-containing TC-NER complex demonstrates that the interaction of STK19 with CSA-DDB1 is critical for repair. Structure prediction-guided mutagenesis further indicates that STK19 also interacts functionally with the XPD subunit of TFIIH. Finally, we identify an interface between the C-terminal tail of CSA and UVSSA that is essential for TC-NER. Together, our results suggest a model of how STK19 promotes TC-NER (Figure 7). The accompanying manuscript by van den Heuvel *et al.* identifies STK19 as an important TC-NER factor in mammalian cells and similarly concludes that it positions TFIIH on the downstream DNA ahead of stalled Pol II.[41]

STK19: lynchpin between TFIIH and stalled Pol II

Previous studies showed that after CSB binds to stalled Pol II, CRL4^{CSA} and UVSSA are recruited and collaborate with ELOF1 to promote Pol II ubiquitination (Figures 7A and 7B).[12] Furthermore, UVSSA was shown to tether TFIIH to the TC-NER complex via its TFIIH-interacting region (TIR; Figure 7C) that we confirm is essential in cell-free TC-NER (Figure 2E). Importantly, because the TIR motif is located in an unstructured part of UVSSA (Figure S7D), the tethered TFIIH has many degrees of freedom (Figure 7C), and it was

unclear how it is positioned on the template strand ahead of Pol II for lesion verification. We propose that after being tethered via UVSSA, TFIIH docks onto STK19 via XPD, which guides TFIIH to the DNA downstream of stalled Pol II (Figure 7D). Subsequently, XPB translocates away from stalled Pol II by tracking along the template strand in the 3'–5' direction, which unwinds DNA, allowing XPD to capture ssDNA in its helicase channel (Figure 7E).[6] Indeed, in the full TC-NER-TFIIH model, the damaged strand in TFIIH is located only ~14 Å from the transcribed strand in Pol II (Figure 5F). Because a charge-swap but not an alanine substitution in the STK19 DNA-binding site impairs TC-NER (Figure 5H), we propose that STK19 must accommodate downstream DNA near the XPD helicase channel to guide the template strand into the ATPase. Notably, STK19 DNA binding mutations were found in cancer patients.[29] Upon ssDNA engagement, XPD translocates in the 5'–3' direction, searching for DNA damage (Figure 7E). When a lesion is located, XPD stalls, followed possibly by further DNA unwinding by XPB,[42,43] dual incisions by XPF-ERCC1 and XPG (Figure 7F), and gap filling (not depicted).

In our model, XPD binding to STK19 would overlap with UVSSA's VHS domain in the TC-NER complex (Figures 7C and 7D; Figures 5A and 5B). Importantly, in addition to the previously reported contact between UVSSA and the β-propeller of CSA (Figure 7C, label I), we find that UVSSA also binds the flexible C-terminal tail of CSA (Figure 7C, label II). Our mutagenesis results further suggest that the latter interaction is more important than the former. Based on these results, we propose that UVSSA dissociation from the CSA β-propeller makes room for XPD to bind STK19, even as UVSSA remains attached to the CSA C-terminus (Figure 7D, label II). In this way, UVSSA first tethers TFIIH to the TC-NER complex and then delivers it to STK19 without allowing TFIIH dissociation.

Interestingly, STK19 depletion reduced repair to a greater extent than the combination of five point mutations targeting the STK19-XPD interface. One explanation of this difference is that these mutations did not fully disrupt the STK19-XPD interaction. Alternatively, STK19 may induce allosteric changes in the TC-NER complex that also enhance repair independently of XPD binding. For example, in the presence of STK19, the UVSSA VHS domain moves towards DNA by 5–8 Å, which might enhance its affinity for the TC-NER complex. In this view, even without a direct XPD-STK19 interaction, TFIIH can eventually find its proper location on the DNA, albeit inefficiently.

Unlike the core TC-NER factors CSB, $CRL4^{CSA}$, and UVSSA, mutations in which give rise to Cockayne syndrome and UV-sensitive syndrome, respectively,[2,12] STK19 and ELOF1 have not yet been linked to these human disorders. If human STK19 mutations should eventually emerge, we speculate they would likely phenocopy defects in UVSSA, and cause mild UV sensitivity, with repair but not Pol II removal by CSB and $CRL4^{CSA}$ being disrupted.

Common themes in transcription initiation, GG-NER, and TC-NER

TFIIH is essential for DNA opening during transcription initiation, GG-NER, and TC-NER.[6] Based on our findings and those of others, we propose that TFIIH function in these three pathways involves at least two common principles. First, the initial recruitment of TFIIH in all three pathways occurs via the PH domain of the p62 subunit. Thus, acidic

sequences in the general transcription factor TFIIE, XPC, and UVSSA bind to the same basic groove in the PH domain with high affinity.[24] The second common principle involves the mechanism of DNA opening by the XPB ATPase subunit of TFIIH. During transcription initiation, XPB translocates along duplex DNA while TFIIH is also anchored to the Pol II stalk.[44,45] This configuration effectively pumps DNA into a gap between the two TFIIH contact points, leading to DNA unwinding. Similarly, in GG-NER, TFIIH is attached via multiple contacts to XPC, which grips the damaged DNA at a distance from XPB.[42] Finally, our data indicate that in the case of TC-NER, TFIIH anchoring involves XPD docking onto the TC-NER complex via STK19 so that XPB pumping DNA towards the stalled polymerase leads to strand separation (Figures 7D and 5F). These considerations argue that both TFIIH recruitment and anchoring are generally required for its function in transcription initiation and repair. Notably, a key difference between these processes is that unlike in transcription initiation, GG-NER and TC-NER require the ATPase activity of XPD,[6] and XPD is positioned immediately adjacent to the DNA (Figure 5D and [42]). As a result, once the duplex is unwound by XPB, one strand readily enters the XPD helicase channel for lesion verification.

A possible function for K1268 ubiquitination in TC-NER

The ubiquitination of RPB1 K1268 stimulates the association of TFIIH with the TC-NER complex, but the underlying mechanism is not understood.[16,39] Our high resolution cryo-EM structure allowed us to model RPB1's K1268 loop. The loop is positioned such that residue K1268 points towards the base of UVSSA's C-terminal helix and the VHS domain (Figure 3H). It is therefore tempting to speculate that RPB1 ubiquitination remodels the loop and surrounding features, and that this promotes the UVSSA VHS domain's repositioning that we propose is essential for XPD binding to STK19. Strikingly, the K1268 loop is also located at the interface with XPD in the composite TC-NER model containing TFIIH (Figure 5F). Our model of TFIIH positioning, together with structural information about K1268's location, sets the stage to address how RPB1 ubiquitination promotes TC-NER.

The power of *in silico* screening for protein-protein interactions

To understand how STK19 functions, we initially used AlphaFold-Multimer (AF-M) to screen for STK19 partners among ~400 proteins involved in genome maintenance and transcription. Given this limited search space, conventional confidence metrics were adequate to identify CSA, XPD, and RPB1 as top candidates. However, SPOC, a classifier trained to identify functionally relevant structure predictions, gave higher relative scores to STK19's functional partners than conventional metrics, consistent with its greater discriminatory power (Figure 3A vs. Figures S3A and S3B). These predictions immediately suggested a hypothesis for STK19's mechanism and allowed us to engineer site-directed mutants that test the model. Subsequently, we determined the cryo-EM structure of the STK19-containing TC-NER complex (Figure 3D), which extended and provided critical experimental support for the structure predictions. This example further illustrates the remarkable synergy between structure prediction and experimental structure determination that accelerates mechanistic discovery.

A cell-free system for TC-NER

The cell-free system we developed recapitulates all key features of TC-NER. Thus, repair requires transcription, all known TC-NER factors, interactions among these factors, and CRL E3 ligase activity. Furthermore, it is strand-specific and accompanied by gap filling. Our approach is ideally suited to address key questions in the field such as the role of ubiquitination and the mechanism of transcription resumption after repair is complete.

Limitations of the study

Although *Xenopus* egg extract recapitulates *bona fide* TC-NER, the maximum efficiency of repair we observed is ~32%. More complete repair may be limited by the percentage of plasmids that are transcribed. Interestingly, we observe a similar maximal repair efficiency for GG-NER, suggesting a common mechanism might limit repair. Using this system, we performed extensive structure-function analyses of recombinant STK19 and other TC-NER factors. Given that STK19 lacks enzymatic activity, verifying proper folding of the mutants was difficult. We therefore verified that all STK19 mutants analyzed eluted at the expected volume compared to wild-type protein in size exclusion chromatography, consistent with proper folding, but unwanted effects of the mutations still cannot be excluded. Despite efforts to observe binding between recombinant *X. laevis* STK19 and XPD, we could not overcome STK19's intrinsic "stickiness", perhaps due to the absence of its various interaction partners in these assays. Nevertheless, the high confidence (Figures 3A and S3A-S3B) and conservation (Figures S3E and S3F) of the AlphaFold prediction for the STK19-XPD interaction, and the fact that mutations engineered on the basis of the predicted interface impaired TC-NER (Figure 5E), suggest that the interaction is physiologically relevant. In the future, it will be important to determine the structure of the TC-NER complex with TFIIH to reveal the intricacies of how STK19 couples Pol II stalling with DNA repair.

RESOURCE AVAILABILITY

Lead contact

Further information and requests for resources and reagents should be directed to and will be fulfilled by the lead contact, Johannes C. Walter (johannes_walter@hms.harvard.edu).

Materials availability

All unique reagents generated in this study are available from the lead contact with a completed materials transfer agreement.

Data and code availability

- Structural coordinates and cryo-EM reconstructions have been deposited at the Electron Microscopy Data Bank (EMDB) and the Research Collaboratory for Structural Bioinformatics Protein Data Bank (RCSB PDB), and will be publicly available as of the date of publication. Their accession codes are listed in the key resources table. Original western blot and gel images will be shared by the lead contact upon request.

- This paper does not report original code.
- Any additional information required to reanalyze the data reported in this paper is available from the lead contact upon request.

STAR★METHODS TEXT

EXPERIMENTAL MODEL AND STUDY PARTICIPANT DETAILS

Xenopus laevis—Experiments involving adult female (Nasco Cat# LM0053MX) and male (Nasco Cat# LM00715MX) *Xenopus laevis* were approved by the Harvard Medical Area Institutional Animal Care and Use Committee (IACUC) and conform to all relevant regulatory standards. All frogs were healthy, maintained at 18°C on a 12-h light cycle and a biweekly feeding schedule. The water was purified by reverse osmosis and conditioned with rock salt approved for aquaculture. Female frogs were handled and ovulated according to approved protocols. Male frogs were not involved in previous procedures.

Insect cell culture: Sf9 cells (Expression Systems, Cat# 94–001S), Tni (Hi5) cells (Expression Systems, Cat# 94–002S), and Sf21 cells (Expression Systems, Cat# 94–003S) were cultured in ESF 921 insect cell culture medium (Expression Systems, Cat# 96–001-01) at 27°C for baculovirus production and protein expression, unless otherwise indicated.

Bacterial cell culture: *E. coli* Rosetta 2(DE3)pLacI (Sigma-Aldrich Cat# 71404–3), OverExpress C41(DE3) (Sigma-Aldrich Cat# CMC0017), DH5α (New England Biolabs (NEB) Cat# C2987H), DH10EMBacY (Geneva Biotech), and BL21-CodonPlus (DE3)-RIL (Agilent Cat# 230245) were cultured in LB broth (EMD-Millipore Cat# 71753–5) at 37°C for plasmid production and protein expression, unless otherwise indicated.

METHOD DETAILS

Preparation of DNA substrates—A plasmid for *in vitro* transcription (pUC18-G5AdML(Δ53)G-) was a generous gift of Stephen Buratowski, and was modified by "Round-the-Horn" PCR using oligos oTM012 and oTM013 to place a tandem BbsI restriction cassette downstream of the promoter for the subsequent introduction of a site-specific DNA lesion. The resulting plasmid pTM07_5xUAS_AdMLΔ53_BbsI, which we refer to as pAdML$^{\Delta 53}$, contains five Upstream Activating Sequences (UAS), a truncated adenovirus major late promoter directly upstream of a G-less cassette, and the BbsI cassette. To increase the transcriptional output, we replaced the AdML$^{\Delta 53}$ as well as the adjacent G-less cassette with a modified super core promoter 2 (SCP2)[57] and a fragment of the *X. laevis* ubiquitin gene by performing Gibson Assembly (NEBuilder HiFi DNA Assembly Master Mix, NEB) using BamHI/SacI-cut pTM07 and gbTM60. This IVT plasmid (pTM171_5xUAS_SCP2*_Ub_BbsI; referred to as pSCP2*) contains a modified SCP2 promoter (referred to as SCP2*) with the Initiator sequence 5'–TCAGTC–3' (instead of 5'–TCAGAC–3') to maximize the use of a single transcription start site (TSS). Additionally, we introduced polyA sites upstream of the 5xUAS to prevent multiple rounds of transcription, and altered the size of the ubiquitin gene using "Round-the-Horn" PCR and oligos oTM376 and oTM377 to position the BbsI cassette at different locations downstream of the TSS. These modifications of pSCP2* generated pCtrl-122 and pCtrl-322. Plasmid

pCtrl-122 was further used to invert the orientation of the BbsI cassette using “Round-the-Horn” PCR and oligos oTM764 and oTM765, generating pCtrl-NTS. Other plasmids used for IVT reactions were ordered from Addgene (pCMV) or described previously (pActin).[34]

The generation of plasmids containing a site-specific cisplatin 1,3-GTG intrastrand crosslink involved the following steps. First, pAdML$^{\Delta 53}$, pCtrl-122, pCtrl-322, and pCtrl-NTS were digested with *BbsI*-HF (NEB) and purified on a HiLoad 16/600 Superdex 200 pg column (Cytiva). Second, the preparation of the lesion-containing insert was performed as described previously.[58] In short, a DNA oligo containing a unique GTG site (oTM016; 5’–CCC TCT CCA CGT GTC TCC TC–3’) was platinated and purified on a Mono Q 5/50 GL column (Cytiva) before it was annealed to the complementary strand (oTM017; 5’–GCA CGA GGA GAC ACG TGG AG–3’). Third, the lesion-containing duplex DNA was ligated into the purified, linear backbones. In the case of large-scale ligation reactions (pAdML$^{\Delta 53}$, pCtrl-122, and pCtrl-322), subsequent purification was performed using CsCl gradient centrifugation and butanol extraction. For the generation of plasmids containing the lesion in the non-template strand (using linearized pCtrl-NTS), small-scale reactions were gel purified using the QIAquick Gel Extraction Kit (Qiagen) prior to purification with AMPure XP Reagent (Beckman), according to manufacturer’s instructions. The final lesion-containing plasmids were verified by *PmlI* restriction digestion, indicating that ~98% (pPt-AdML$^{\Delta 53}$, pPt-122, and pPt-322) or ~92% (pPt-NTS) of the plasmids contained the crosslink. Lesion plasmids were frozen in liquid nitrogen and stored at −80°C.

Xenopus* egg extract preparation—Xenopus laevis* egg extracts (HSS, high-speed supernatant; NPE, nucleoplasmic extract) were prepared as follows[59]. Female frogs were primed with 37.5 IU of human Chorionic Gonadotropin (hCG, CHORULON) (Merck, Cat# 22219) 3–6 days before egg extract preparation. To induce ovulation, 625 IU of hCG was injected 20–23 h prior to collecting eggs. HSS was prepared from six female frogs, and NPE was prepared from 20 female frogs. Sperm chromatin required for NPE preparations was purified from male frog testes. Eggs were collected, dejellied, and crushed at 20,000 ß g. Crude egg lysate was recovered and either centrifuged at 260,000 x g to make HSS, which was frozen at −80°C, or processed for NPE production. To make NPE, crude lysate was supplemented with ATP regenerating system and sperm chromatin (final concentration 4,400/µl). After allowing nuclear assembly for 70–80 minutes, nuclei from ~8 ml aliquots of assembly reaction were floated to the top of 13×100 mm plastic tubes at 20,000 ß g for 2 minutes, harvested from the top of the tube with a cut-off pipette tip, and recentrifuged at 260,000 ß g to separate chromatin and nuclear envelopes from the NPE. NPE was harvested, frozen in liquid nitrogen, and stored at −80°C.

***In vitro* transcription (IVT) assay—**Thawed *Xenopus* egg extracts were supplemented with ATP regenerating system (2 mM ATP, 20 mM phosphocreatine, and 5 µg/ml phosphokinase; final concentrations), 2 mM DTT (only NPE), and 3 µg/ml nocodazole (only HSS). HSS was cleared by centrifugation at 14,000 ß g for 5 min at room temperature prior to IVT reactions. Where indicated, recombinant transcription activator GAL4-VP64 (1 µM final concentration in IVT reaction), recombinant human TBP (500 nM), and α-amanitin (2 µM) were added to egg extracts. The resulting “Extract Mixture” was incubated for 15

min at room temperature. In parallel, an “IVT Mixture” was prepared with the following components: 10ß IVT Buffer–100 (200 mM HEPES pH 7.5, 1 M KCl, 50 mM $MgCl_2$, and 5 mM EDTA; 1x final concentration in IVT reaction), Recombinant RNasin Ribonuclease Inhibitor (Promega; 0.5 U/µl), indicated IVT plasmid (7 ng/µl), [α−^{32}P]UTP (Revvity; 0.5 µCi/µl), and, unless otherwise indicated, polyethylene glycol 20,000 (PEG^{20K}; Hampton Research; 1% (v/v)).

To initiate IVT reactions, “Extract Mixture” and “IVT Mixture” were combined such that egg extracts (supplemented with ATP regenerating system and DTT or nocodazole) represent 50% of the final reaction volume. Reactions were incubated at room temperature. At indicated times, samples were withdrawn and mixed with seven volumes of IVT Stop Solution (50 mM Tris pH 8.0, 25 mM EDTA, and 0.5% SDS) and treated with 1.2 mg/ml Proteinase K (Roche) for 1 h at 37°C. RNA transcripts were then purified using RNAClean XP (Beckman), according to manufacturer’s instructions, except that two volumes of bead solution were added and RNA was eluted with TE Buffer. Eluted RNA transcripts were mixed with 2x IVT Loading Buffer (100% formamide supplemented with 1 mM EDTA, 0.1% SDS, 1 µg/ml Xylene Cyanol FF, and 1 µg/ml Bromophenol Blue), heated to 95°C for 5 min, rapidly cooled on ice, and resolved on an 8% Urea-PAGE gel in 0.8x Glycerol Tolerant Gel Buffer (20x stock: 1.78 M Tris, 0.57 M taurine, 0.01 M EDTA). Gels were dried under vacuum, exposed to a phosphor screen, and imaged on a Typhoon FLA 7000 phosphorimager (GE Healthcare). RNA transcripts in Figures 1B and S1B were purified by conventional phenol-chloroform extraction and ethanol precipitation instead of using RNAClean XP beads.

Cell-free TC-NER assay—The repair of plasmids containing a cisplatin 1,3-GTG intrastrand crosslink was performed under IVT assay conditions, with the following changes. The “IVT Mixture” contained 10x IVT Buffer–33 (200 mM HEPES pH 7.5, 330 mM KCl, 50 mM $MgCl_2$, and 5 mM EDTA; 1ß final concentration in IVT reaction) instead of 10x IVT Buffer–100, damaged IVT plasmid (10 ng/µl instead of 7 ng/µl), and no [α−^{32}P]UTP. For monitoring UDS (Figure 2H), [α−^{32}P]dCTP (Revvity; 0.8 µCi/µl) was added. For experiments shown in Figures 1C, 1D and S1E, the “Extract Mixture” was prepared with undepleted NPE, and, where indicated, GG-SNER was inhibited by the addition of XPC antibody (1.5 µM final concentration). For all other cell-free repair assays, NPE was first immunodepleted of XPC and the indicated factors (see protocol below), unless indicated otherwise. Compared to IVT assays, the “Extract Mixture” for cell-free repair was further supplemented with a 17.5x stock of “CSB Mixture” and a 11.67x stock of “CSA Mixture” (both used at 1ß in the final repair reaction). The “CSB Mixture” contained CSB Buffer (50 mM HEPES pH 7.5, 300 mM NaCl, 10% (v/v) glycerol, and 2 mM DTT) and, where indicated, recombinant hsCSB, xlELOF1, and xlSTK19 variants. The “CSA Mixture” contained CSA Buffer (25 mM HEPES pH 7.5, 150 mM NaCl, 5% (v/v) glycerol, and 2 mM DTT) and, where indicated, recombinant xlCSA-xlDDB1 (or $CRL4^{CSA}$; both can be used interchangeably; not shown) and xlUVSSA. Final repair reactions generally contained the following concentrations of recombinant TC-NER factors: 200 nM CSB, 100 nM CSA-DDB1, 200 nM ELOF1, 200 nM STK19, and ~50 nM UVSSA. Instead of adding the CSA-DDB1 heterodimer, the assays described in Figures 1D–1F as well as the

majority of experiments conducted for Figures 2A and 2B were performed with recombinant $CRL4^{CSA}$, which was assembled from purified CSA-DDB1 and CUL4A-RBX1 dimers. We did not observe any detectable difference in the TC-NER activity of the two CSA complexes. As an alternative to using purified *X. laevis* UVSSA, wild-type and mutant proteins could be produced in the TnT SP6 High-Yield Wheat Germ Protein Expression System (Promega) according to manufacturer's instructions, which was then added directly to the "Extract Mixture" in an amount comprising up to 12% of the final reaction. For the experiment shown in Figure 2F, the cullin inhibitor MLN4924 was supplemented at a final concentration of 200 μM in the "Extract Mixture".

Once the complete "Extract Mixtures" were prepared, samples were withdrawn for western blot analyses shown in Figures S2C-S2K. Repair reactions were started by combining "Extract Mixture" and "IVT Mixture" such that NPE (supplemented with ATP regenerating system and DTT) represents 50% of the final reaction volume. Reactions were incubated at room temperature for the indicated times, when samples were withdrawn and mixed with seven volumes of IVT Stop Solution containing 0.25 mg/ml RNase A. After 30 min incubation at 37°C, Proteinase K was added to 1.2 mg/ml, and samples were incubated for 1 h at 37°C. Plasmids were then purified using AMPure XP Reagent (Beckman), according to manufacturer's instructions, except that 1.8 volumes of bead solution were added. The DNA was eluted and digested with the appropriate restriction enzyme mix prepared in 1x rCutSmart buffer (NEB) for 1 h at 37°C. For the UDS assay in Figure 2H, *EcoRI*-HF and *KpnI*-HF were added, samples were stopped with 2x IVT Loading Buffer, denatured for 5 min at 95°C, resolved on a 10% Urea-PAGE gel in 0.8x GTG buffer, vacuum dried, and visualized by autoradiography as described above. For error-free repair experiments, the DNA was digested with *XhoI* and *PmlI* and subsequently stopped with Replication Stop Solution (80 mM Tris [pH 8.0], 8 mM EDTA, 0.13% phosphoric acid, 10% Ficoll, 5% SDS, and 0.2% bromophenol blue). Reactions containing wheat germ extract were digested with *AflII* in addition to *XhoI* and *PmlI* to linearize the expression plasmid to not interfere with the damaged and repaired DNA fragments. DNA products were resolved on a native 0.9% agarose gel in 1x TBE, stained with SYBR Gold (Invitrogen) and imagen on a Typhoon 5 (GE Healthcare). The smaller DNA digestion product after repair (see schematic in Figure 1A) was often fuzzy and not much more intensely stained than the background (see Figure 1C). Therefore, only the larger DNA product after repair, as well as the remaining damaged DNA fragment, were quantified using ImageJ (NIH) as described below in the Quantification and Statistical Analysis section.

Antibodies and immunodepletions—Rabbit polyclonal antibodies against the following *X. laevis* peptides were raised and affinity-purified by Biosynth, and used for both western blotting and immunodepletions unless otherwise indicated: XPC CT (C-terminal amino acids 1049–1062; Ac-CKKGEENHLFPFEKL-OH; used for GG-NER inhibition), XPC NT (N-terminal amino acids 1–20; H_2N-MAKRGSSEGAAVAKKKPRKQC-amide; used for XPC immunodepletion and XPC purification), CSB (amino acids 1357–1370; Ac-CIDGTGVWRLKPEFH-OH; for western blotting only); CSA (amino acids 380–399; Ac-CHRTHINPAFEDAWSSSEDES-OH),[15] UVSSA (amino acids 718–737; Ac-CNRADKSRHEKFANQFNYALN-OH), STK19 (amino

acids 1–15; H_2N-MDRKRKLISDAFKVKC-amide; peptide sequence contains a cysteine 9 to serine substitution), RPB1 (four heptad repeats of the C-terminal domain; Ac-C$(YSPTSPS)_4$-amide; used for western blotting), and XPD (amino acids 741–760; Ac-CLEQLQSEEMLQKIQEIAHQV-OH; used for western blotting). Rabbit polyclonal antibodies against full-length *X. laevis* ELOF1 were prepared by Pocono Rabbit Farm and Laboratory, affinity-purified from serum using the recombinant ELOF1 coupled to AminoLink Coupling Resin (Thermo Fisher Scientific) according to manufacturer's protocol, and used for western blotting and immunodepletions. The following antibodies were used for western blotting: Rabbit polyclonal antibody against *X. laevis* TDG,[47] and rat monoclonal antibodies targeting RPB1 phospho-Ser5 (clone 3E8) and phospho-Ser2 (clone 3E10), which were a generous gift of Stephen Buratowski.

Immunodepletions were performed with (i) rProtein A Sepharose Fast Flow (Cytiva), (ii) Dynabeads Protein A for Immunoprecipitation (Invitrogen), or (iii) Protein A Mag Sepharose Xtra (Cytiva) after equilibration with 1x PBS supplemented with 0.25 mg/ml BSA (and 0.05% Tween in case of (iii)). For (i), five volumes of affinity-purified antibodies (1 mg/ml) were incubated with one volume of beads. For (ii), one volume of affinity-purified antibodies (1 mg/ml) were incubated with two volumes of bead slurry. For (iii), two volumes of affinity-purified antibodies (1 mg/ml) were incubated with one volume of bead slurry. After gentle rotation overnight at 4°C, beads were washed three times with 1x PBS supplemented with 0.1 mg/ml BSA (and 0.05% Tween in case of (iii)) and three times with egg lysis buffer (ELB; 10 mM HEPES [pH 7.7], 50 mM KCl, 2.5 mM $MgCl_2$, and 250 mM sucrose) supplemented with 0.1 mg/ml BSA. Three rounds of depletion were then performed for one hour each at 4°C by incubating one volume of antibody-bound beads or bead slurry with 5 (i), 0.75 (ii), or 2 (iii) volumes of egg extract. The depleted extracts were collected and immediately used for IVT, GG-NER, or TC-NER assays as described above.

SDS-PAGE and immunoblotting—Extract samples were stopped with 2x Laemmli sample buffer (120 mM Tris [pH 6.8], 4% SDS, 20% glycerol, 0.02% bromophenol blue, and 10% β-mercaptoethanol), boiled for 2 min at 95°C, and resolved on 4–15% Mini-PROTEAN TGX Precast Protein Gels or 4–15% Criterion TGX Precast Midi Protein Gels (Bio-Rad) using Tris-Glycine-SDS Running Buffer (Boston BioProducts). InstantBlue Protein Stain (Novus) was used for coomassie staining. For western blotting, gels were transferred to PVDF membranes (Perkin Elmer). Membranes were blocked with 5% (w/v) non-fat milk in PBST for 30–60 min at room temperature. Primary antibodies were diluted 1:500 – 1:5,000 in 1x PBST supplemented with 1% BSA and 0.02% sodium azide. After overnight incubation at 4°C, membranes were extensively washed with 5% (w/v) non-fat milk in PBST at room temperature prior to incubation with horseradish peroxidase (HRP)-conjugated secondary antibodies (Jackson ImmunoResearch) diluted to 1:10,000 in 5% (w/v) non-fat milk in PBST. After secondary antibody incubation for 45–60 min at room temperature, membranes were washed with 1x PBST, incubated with SuperSignal West Dura Extended Duration Substrate (Thermo), and imaged on an Amersham Imager 600 (GE Healthcare).

Cloning of TC-NER factors used in cell-free TC-NER—Sequences encoding *H. sapiens* STK19 as well as *X. laevis* STK19, UVSSA, and CSA were ordered as codon-optimized gBlocks from Integrated DNA Technologies (IDT). Open reading frames for UVSSA (gbTM07) and CSA (gbTM129 and gbTM130) were separately cloned into pAceBac1 (pAB1), introducing an N-terminal FLAG tag on UVSSA (pTM81) and leaving CSA untagged. DDB1 was cloned from cDNA (HMS DNA core; ID XlCD00441616) into pAB1, introducing an N-terminal His6 tag, followed by a TEV protease cleavage site and an Avi tag. Both CSA and DDB1 plasmids were combined into a single plasmid by I-CeuI restriction digest of the CSA-containing plasmid and PCR amplification of the DDB1-containing plasmid with oligos oTM689 and oTM690 using Gibson Assembly (NEBuilder HiFi DNA Assembly Master Mix, NEB), yielding pTM449. *X. laevis* UVSSA was also cloned into the pF3A backbone (Promega #L5671) for expression in the TnT SP6 High-Yield Wheat Germ Protein Expression System (Promega) using oligos oTM405 and oTM406 and pTM81 as the template. Subsequently the FLAG tag was removed using oTM422 and oTM423, yielding pTM240. Using Gibson Assembly, open reading frames for both *H. sapiens* (gbTM93) and *X. laevis* (gbTM74) STK19 were directly cloned into pOPINB (Addgene #41142), introducing a PreScission protease cleavable N-terminal His6 tag. *X. laevis* (gbTM74) STK19 was also cloned into pOPINK (Addgene #41143), featuring a PreScission protease cleavable N-terminal His6-GST tag. In hsSTK19, four internal, previously misannotated residues (Val112, Cys113, Asp114, Cys115) were subsequently removed by PCR using oligos oTM569 and oTM570, yielding pTM365. Point mutations and truncations of STK19, UVSSA, ELOF1, and CSA were introduced by “Round-the-Horn” mutagenesis using Q5 Hot Start High-Fidelity 2X Master Mix (NEB) and oligos listed in Table S4. All plasmids were verified by Sanger or whole plasmid sequencing.

Protein expression and purification for cell-free transcription and repair—All purifications were performed at 4°C unless stated otherwise. *H. sapiens* CSB variants and *X. laevis* CUL4A-RBX1 were recombinantly expressed in insect cells and purified as described.[15] In short, cleared Sf9 cell lysates were incubated with ANTI-FLAG M2 Affinity Gel (Millipore) to purify FLAG-hsCSB and FLAG-xlCUL4A-xlRBX1, respectively. After elution with 3x FLAG Peptide (Sigma), CSB was further purified by gel filtration on a Superdex 200 Increase 10/300 GL (Cytiva) column, whereas CUL4A-RBX1 was directly dialyzed, concentrated, frozen in liquid nitrogen, and stored at −80°C.

X. laevis UVSSA and CSA-DDB1 variants were expressed in insect cells. Bacmids were produced and Sf9 cells were maintained and propagated as described previously.[15] Protein expression was performed in Sf9 (UVSSA) or Hi5 (CSA-DDB1) cells for 72 h at 27°C (UVSSA) or 20°C (CSA-DDB1). Harvested cell pellets were resuspended in respective lysis buffer (see below), frozen in liquid nitrogen, and stored at −80°C prior to purification. Cells were thawed in a water bath, supplemented with one tablet cOmplete EDTA-free Protease Inhibitor Cocktail (Roche), lysed by sonication, and cleared by centrifugation for 1 h at 35,000 rpm in a Beckman Ti45 rotor.

The N-terminally FLAG tagged UVSSA was purified using ANTI-FLAG M2 Affinity Gel (Millipore) equilibrated in UVSSA Lysis Buffer (50 mM HEPES pH 7.5, 500 mM NaCl, 10% glycerol, and 0.1% NP-40). The cleared and filtered (0.8-μm syringe filter) lysate was

incubated with the resin for 2 h at 4°C before washing with UVSSA Wash Buffer (50 mM HEPES pH 7.5, 500 mM NaCl, and 10% glycerol). The resin was equilibrated with UVSSA Buffer (25 mM HEPES pH 7.5, 150 mM NaCl, and 5% glycerol) and eluted with UVSSA Buffer containing 0.2 mg/ml 3x FLAG Peptide (Sigma). Peak fractions were pooled, DTT was added to a final concentration of 2 mM, the protein was concentrated with a 0.5 ml 10 MWCO spin concentrator (Millipore), frozen in liquid nitrogen, and stored at −80°C.

The CSA-DDB1 heterodimer was purified by applying the cleared and filtered lysate to a 5 ml HisTrap HP column (Cytiva) that was equilibrated in CSA Lysis Buffer (25 mM HEPES pH 7.5, 150 mM NaCl, 10% glycerol, 2 mM 2-mercaptoethanol, and 20 mM imidazole). The column was washed with 4 column volumes (CV) CSA Lysis Buffer, 10 CV CSA High Salt Buffer (CSA Lysis buffer, except 800 mM NaCl), and 4 CV CSA Lysis Buffer. At this point, a 1 ml HiTrap Q HP column (Cytiva) was connected downstream of the HisTrap HP column, and the protein was eluted directly onto the HiTrap Q column with 3 CV CSA Elution Buffer (CSA Lysis buffer, except 300 mM imidazole). The columns were subsequently washed with 3 CV CSA Lysis Buffer prior to the removal of the HisTrap HP column. The protein was eluted from the HiTrap Q column with a linear gradient from CSA Lysis Buffer to CSA High Salt Buffer over 25 CV. Peak fractions were collected, mixed with TEV protease, and dialyzed O/N against CSA Lysis Buffer. The sample was applied to the regenerated and pre-equilibrated HisTrap HP column, and the flow-through was collected, concentrated with a 5 ml 50 MWCO spin concentrator, and loaded onto a Superdex 200 Increase 10/300 GL (Cytiva) equilibrated in CSA Buffer (25 mM HEPES pH 7.5, 150 mM NaCl, 5% (v/v) glycerol, and 2 mM DTT). Peak fractions were pooled, concentrated with 5 ml 50 MWCO spin concentrator (Millipore), frozen in liquid nitrogen, and stored at −80°C.

H. sapiens and *X. laevis* STK19 variants as well as *X. laevis* ELOF1 variants, GAL4-VP64, and H. sapiens TBP were recombinantly expressed in *E. coli* OverExpress C41(DE3) Chemically Competent Cells (Sigma) or Rosetta 2(DE3)pLacI Competent Cells (Sigma) grown at 37°C in LB media supplemented with the appropriate antibiotics. Typically, 2 l per construct were expressed. At an OD 600 of 0.5–0.7, protein expression was induced with 0.5 mM IPTG, and cultures grown for 18–20 h at 18°C. Cells were harvested by centrifugation, resuspended in the respective lysis buffer (see below), frozen in liquid nitrogen, and stored at −80°C. To start the purification, cells were thawed in a water bath, supplemented with 1 mg/ml lysozyme and one tablet cOmplete EDTA-free Protease Inhibitor Cocktail (Roche), opened by sonication, and cleared by centrifugation for 1 h at 35,000 rpm in a Ti45 rotor (Beckman).

X. laevis STK19 and ELOF1 expressed with a PreScission protease cleavable N-terminal His6-GST tag was purified using Glutathione Sepharose 4B resin (Cytiva) equilibrated with Lysis Buffer (25 mM HEPES pH 7.5, 300 mM NaCl, 10% (v/v) glycerol, and 2 mM DTT). After incubation for 1 h at 4°C, the resin was washed extensively with Lysis Buffer prior to cleavage of the His6-GST tag on the resin with GST-tagged PreScission protease overnight at 4°C. The released, untagged STK19 and ELOF1 was collected and subjected to size-exclusion chromatography on a HiLoad 16/600 Superdex 75 pg column (Cytiva) equilibrated in Lysis Buffer. Peak fractions were pooled, concentrated, snap-frozen in liquid nitrogen, and stored at −80°C.

H. sapiens and *X. laevis* STK19 variants expressed with a PreScission protease cleavable N-terminal His6 tag were purified using Ni-NTA Superflow resin (Qiagen) equilibrated in STK19 NiNTA Buffer (50 mM HEPES pH 7.5, 300 mM NaCl, 10 mM imidazole, 10% (v/v) glycerol, and 2 mM 2-mercaptoethanol). Incubation for 1 h at 4°C was followed by extensive washing of the beads with STK19 NiNTA Wash Buffer (50 mM HEPES pH 7.5, 500 mM NaCl, 20 mM imidazole, 10% (v/v) glycerol, and 2 mM 2-mercaptoethanol). Proteins were eluted with STK19 NiNTA Buffer containing 300 mM imidazole. His-STK19 variants were directly subjected to size-exclusion chromatography on a HiLoad 16/600 Superdex 75 pg column (Cytiva) equilibrated in STK19 Buffer. Untagged human STK19 was dialyzed against STK19 Buffer after NiNTA elution in the presence of GST-tagged PreScission protease. On the next day, the sample was concentrated and directly subjected to size-exclusion chromatography on a HiLoad 16/600 Superdex 75 pg column (Cytiva) that had a 1 ml GSTrap HP column (Cytiva) attached downstream. Peak fractions were pooled, concentrated with a 5 ml 10 MWCO spin concentrator, frozen in liquid nitrogen, and stored at −80°C.

The transcription activator GAL4-VP64 and *H. sapiens* TBP were also expressed with an N-terminal His6 tag, but without a PreScission protease site. Purifications were performed analogously and featured the same affinity and size-exclusion steps.

X. laevis XPC used in Figure S1 was purified from egg extract (HSS; high-speed supernatant) using a polyclonal antibody that was raised against the XPC N-terminus (see above). The antibody was immobilized on rProtein A Sepharose Fast Flow (Cytiva) and then incubated with HSS overnight at 4°C. The beads were washed with Wash Buffer (25 mM HEPES pH 7.5, 0.1 mM EDTA, 12.5 mM MgCl2, 10% glycerol, 0.1 mM DTT and 0.01% NP-40) supplemented with 400 mM KCl followed by Wash Buffer supplemented with 200 mM KCl. The endogenous XPC protein was eluted with Wash Buffer containing 200 mM KCl and 1.5 mg/ml XPC NT peptide (H_2N-MAKRGSSEGAAVAKKKPRKQC-amide; Biosynth). The eluted sample was subjected to size exclusion chromatography on a Superose 6 Increase column (Cytiva) equilibrated with XPC SEC Buffer (25 mM HEPES pH 7.5, 150 mM NaCl, 10% glycerol, and 2 mM DTT). Peak fractions were pooled, concentrated with a 5 ml 10 MWCO spin concentrator (Millipore), frozen in liquid nitrogen, and stored at −80°C.

AF-M Model Generation—Unless otherwise stated, AlphaFold-Multimer (AF-M)[60] structure predictions were generated using ColabFold 1.5[61] running AF-M with v2.3 weights, 1 ensemble, 3 recycles, templates enabled, without dropout, and with maximum Multiple Sequence Alignments MSA depth settings (max_seq = 508, max_extra_seq = 2048). MSAs (paired and unpaired) were provided to AlphaFold-Multimer via the MMSeq2[62] API built into ColabFold.

AF-M Model Analysis—Analysis of structural predictions generated by AF-M was performed using python scripts as previously described.[36,63] Briefly, confident interchain residue contacts were extracted from structures by identifying proximal residues (distance <5 Å) where both residues have pLDDT values >50 and PAE score <15 Å. All subsequent downstream analysis of interface statistics (average pLDDT, average PAE) were calculated

using data associated with these inter-residue pairs (contacts). Average interface pLDDT values above 70 are generally considered confident.[64] The average models score was calculated by averaging how many independent AF-M models predicted a contact across all unique inter-residue contact pairs. This number was then normalized by dividing the number of models run to produce a final score that ranges from 0 (worst) to 1 (best). An average models score above 0.5 is considered confident. pDOCKQ estimates of interface accuracy scores were calculated independently of the contact analysis described above using code from [65]. pDOCKQ values above 0.23 are considered confident.

SPOC Analysis—A random forest classifier (Structure Prediction and Omics Classifier) SPOC trained to distinguish biologically relevant interacting protein pairs from non-relevant interaction pairs was run on AF-M predictions as described previously.[36] For every interaction evaluated, it generates a score that can range from 0 (worst) to 1 (best). Higher scores indicate that AF-M interface metrics and several types of externally sourced biological data are consistent with the existence of the binary interaction tested. SPOC scores above 0.5 are generally associated with high confidence interaction predictions.

Biolayer interferometry (BLI)—DNA binding experiments were performed on an Octet RED384 system (Sartorius). A 5'-biotinylated 14mer (oTM626; 5'–Biotin–TATGGACAGCAAGC–3') was mixed and annealed with a complementary 14mer (oTM629; 5'–GCTTGCTGTCCATA–3') in Annealing Buffer (10 mM Tris pH 7.5, 50 mM NaCl, and 1 mM EDTA). The DNA duplex was captured at a concentration of 1.25 μg/ml in BLI Buffer (ELB containing 0.05% Tween-20 and 5 mg/ml BSA) on an Octet Streptavidin (SA) Biosensor (Sartorius). His-tagged *X. laevis* STK19 variants were diluted to 500 nM in BLI Buffer. Binding to the immobilized DNA duplex was conducted in parallel in Octet 384 Well Tilted Bottom Plates (Sartorius) at 30°C, shaking at 1,000 rpm, using the following steps: 120 s baseline (BLI Buffer), 120 s sample (DNA duplex) loading, 120 s baseline (BLI Buffer), 300 s analyte (STK19) association, 600 s dissociation. The data was processed in Octet Analysis Studio 13.0. To combine the detected absolute responses from multiple independent experiments, relative responses in each experiment were calculated using the STK19 wild-type response at the end of the association phase (300 s), which was given the value 1. The data was analyzed and plotted in GraphPad Prism (version 10.2.2).

In vitro* ubiquitination assays—X. laevis* $CRL4^{CSA}$ complexes were assembled by incubating equimolar amounts of purified CSA-DDB1 variants with CUL4A-RBX1 for 15 min at room temperature. Complexes were then neddylated using the NEDD8 Conjugation Initiation Kit (R&D Systems) according to the manufacturer's instructions, except using reduced final concentrations for Uba3 (0.5x), UbcH12 (0.5x), and NEDD8 (0.33x). After 30 min incubation at room temperature, ubiquitination reactions were prepared in Ubiquitination Buffer (40 mM Tris pH 7.5, 10 mM $MgCl_2$, 0.6 mM DTT), and contained the following proteins: 100 nM E1 enzyme (R&D Systems), 1 μM E2 enzyme (UBE2E1 for UVSSA monoubiquitination or UBE2D2 for CSB polyubiquitination; UBPBio), 1 μM of the indicated neddylated $CRL4^{CSA}$ variant, 25 μM ubiquitin, and 400 nM substrate (UVSSA or CSB). Reactions were started by the addition of 10 mM ATP, incubated at room temperature for the indicated times, stopped with 2x Laemmli sample buffer, and

analyzed by SDS-PAGE and western blotting. Samples of the UVSSA monoubiquitination assay were resolved on a 7.5% Mini-PROTEAN TGX Precast Protein Gel, whereas CSB polyubiquitination was analyzed on a 4–15% SDS-PAGE gel, as described above.

Cloning of human TC-NER factors—*H. sapiens* TC-NER factors were cloned into the 438-series vectors or the 1-series vectors (MacroLab vectors, UC Berkeley). Initial ORFs were obtained by PCR amplification from cDNA or by synthesis of gBlocks (IDT DNA Technologies) using oligos and gBlocks listed in Table S4. The ORFs were subsequently introduced in the respective vectors using ligation-independent cloning. CSB was tagged with an N-terminal His6 tag, followed by a TEV protease cleavage site (vector 438-B). CSB, amplified from cDNA, had three amino acid variants compared to the canonical isoform (V1097M, G1213R, and R1413Q). None of the three amino acid variants are resolved in our structure or impact reconstitution of TC-NERS. UVSSA was tagged with an N-terminal His6 tag, followed by a TEV protease cleavage site (vector 438-B). CSA was cloned with no tag (vector 438-A). DDB1 was tagged with an N-terminal His6 tag, followed by a TEV protease cleavage site (vector 438-B). The DDB1 and CSA vectors were subsequently combined into a multi-ORF plasmid using ligation-independent cloning. DDA1 was tagged with an N-terminal His6 tag, maltose binding protein (MBP) tag, a 10-residue asparagine linker, and a TEV protease cleavage site.

Protein expression and purification of *S. scrofa* RNA polymerase II and *H. sapiens* TC-NER factors—Plasmid propagation and bacmid isolation were performed in *E. coli* DH5α (plasmid propagation) or *E. coli* DH10 EMBacY (bacmid isolation). Recombinant protein expression in insect cells was performed using Sf9, Sf21, and Hi5 cell lines as outlined above and described.[66] Recombinant expressions in insect cells were harvested after 72 hours. Recombinant protein expressions in insect cells or *E. coli* were centrifuged to harvest. Cell pellets were resuspended in respective lysis buffer (see below), flash-frozen, and stored at −80°C prior to purification.

H. sapiens CSB, UVSSA, and CSA-DDB1 were recombinantly expressed in insect cells. DDA1 and ELOF1 were recombinantly expressed in *E. coli* BL21-CodonPlus (DE3)-RIL (Agilent). Specifically, 4 L or 6 L of 2X YT media were inoculated with DDA1 or ELOF1 overnight culture under appropriate antibiotic selection. At OD 600, protein expression was induced with 1 mM of IPTG. Cells were grown at 37°C for three hours before harvest via centrifugation.

Sus scrofa RNA polymerase II was purified from pig thymus.[67] Pig thymus was homogenized and clarified by centrifugation. The sample was subsequently PEI precipitated and resolubilized using a high salt buffer. The resolubilized sample was applied to a MacroQ, followed by ammonium sulphate precipitation and an antibody-based purification (8WG16). Elution fractions containing RNA polymerase II were applied to a UnoQ and eluted using a salt gradient. The sample was subsequently dialyzed, concentrated, aliquoted and flash frozen. The sample was stored at −80°C.

H. sapiens ELOF1 was purified essentially as described.[19] In short, cell pellets were lysed by sonication, cleared by centrifugation, and cleared by filtration. The lysate was

applied to a HisTrap column, followed by washes and elution using a linear imidazole gradient. Peak fractions containing ELOF1 were pooled, treated with TEV protease, and dialyzed overnight. The sample was reapplied to a HisTrap column to remove TEV protease and undigested protein. Unbound ELOF1 fractions were concentrated, applied to a size exclusion column (Superdex 75), pooled, concentrated, aliquoted, flash frozen, and stored at −80°C. The expression and purification of *H. sapiens* STK19 was described above.

All *H. sapiens* TC-NER factor protein purifications were performed at 4°C, unless otherwise specified. The purity of protein preparations was assessed using SDS–PAGE with NuPAGE 4–12% Bis-Tris protein gels (Invitrogen) followed by OneStep Blue (Biotium) staining. Cells were thawed in a water bath. Following cell lysis by sonication, the lysate was clarified using centrifugation and subsequent ultracentrifugation. The supernatant was then filtered using 0.8-μm syringe filters. All protein concentrations were determined by measuring absorption at 280 nm and using the predicted extinction coefficient for the protein(s).

For *H. sapiens* CSB, the filtered supernatant was applied to a 5 mL HisTrap HP column (Cytiva) equilibrated in lysis buffer (500 mM NaCl, 20 mM Na-HEPES pH 7.4, 10% (v/v) glycerol, 30 mM imidazole pH 8.0, and 5 mM 2-mercaptoethanol, 0.284 μg ml−1 leupeptin, 1.37 μg ml−1 pepstatin A, 0.17 mg ml−1 PMSF, and 0.33 mg ml−1 benzamidine). The column was washed with 5 column volumes (CV) of lysis buffer, followed by 20 CV of High Salt buffer (1 M NaCl, 20 mM Na-HEPES pH 7.4, 10% (v/v) glycerol, 30 mM imidazole pH 8.0, and 5 mM 2-mercaptoethanol, 0.284 μg ml−1 leupeptin, 1.37 μg ml−1 pepstatin A, 0.17 mg ml−1 PMSF, and 0.33 mg ml−1 benzamidine). The column was subsequently washed with 5 CV of lysis buffer and the protein was eluted with a 20 CV linear gradient from 0% to 100% Elution buffer (lysis buffer with 500 mM imidazole). Peak fractions were pooled, mixed with TEV protease and dialyzed overnight in 7 kDa MWCO SnakeSkin dialysis tubing (Thermo Scientific) against dialysis buffer (500 M NaCl, 20 mM Na-HEPES pH 7.4, 10% (v/v) glycerol, 50 mM imidazole pH 8.0, and 5 mM 2-mercaptoethanol, 0.284 μg ml−1 leupeptin, 1.37 μg ml−1 pepstatin A, 0.17 mg ml−1 PMSF, and 0.33 mg ml−1 benzamidine). The protein was then applied to tandem HisTrap/HiTrap Heparin HP (5 ml each) columns (Cytiva) equilibrated in dialysis buffer. The columns were washed with 5 CV of dialysis buffer after which the HisTrap column was removed. The protein was eluted off the HiTrap Heparin HP column using a 20 CV long linear gradient from 0% dialysis buffer to 100% high salt buffer. Peak fractions were pooled and concentrated with 100 kDa MWCO Amicon Ultra Centrifugal Filters (Merck) and applied to a Superdex 200 Increase 10/300 GL (Cytiva) column equilibrated in gel filtration buffer (500 mM NaCl, 20 mM Na-HEPES pH 7.4, 10% (v/v) glycerol, and 1 mM TCEP). Fractions containing CSB were concentrated with a 100 kDa MWCO Amicon Ultra Centrifugal Filters (Merck). Protein concentration was determined as described and CSB was aliquoted, flash-frozen, and stored at −80°C.

For *H. sapiens* UVSSA, the filtered supernatant was applied to a 5 ml HisTrap HP column equilibrated in lysis buffer. The column was washed with 5 CV of lysis buffer (500 mM NaCl, 20 mM Na-HEPES pH 7.4, 10% (v/v) glycerol, 30 mM imidazole pH 8.0, and 5 mM 2-mercaptoethanol, 0.284 μg ml−1 leupeptin, 1.37 μg ml−1 pepstatin A, 0.17 mg ml−1 PMSF, and 0.33 mg ml−1 benzamidine), followed by 20 CV of high salt buffer (1

M NaCl, 20 mM Na-HEPES pH 7.4, 10% (v/v) glycerol, 30 mM imidazole pH 8.0, and 5 mM 2-mercaptoethanol, 0.284 μg ml−1 leupeptin, 1.37 μg ml−1 pepstatin A, 0.17 mg ml−1 PMSF, and 0.33 mg ml−1 benzamidine). The column was washed with 5 CV of Lysis buffer and 5 CV of low salt buffer (150 mM NaCl, 20 mM Na-HEPES pH 7.4, 10% (v/v) glycerol, 30 mM imidazole pH 8.0, and 5 mM 2-mercaptoethanol, 0.284 μg ml−1 leupeptin, 1.37 μg ml−1 pepstatin A, 0.17 mg ml−1 PMSF, and 0.33 mg ml−1 benzamidine). After washing, a HiTrap Q HP (5 ml) column (Cytiva, equilibrated in low salt buffer) was attached to the HisTrap HP column. The protein was eluted onto the HiTrap Q HP with a 10 CV step gradient of 100% elution buffer (lysis buffer supplemented with 500 mM imidazole). The HisTrap HP column was then removed, and the HiTrap Q column was washed with 5 CV of low salt buffer. The protein was eluted off the HiTrap Q HP column using a 20 CV long linear gradient from 0% low salt buffer to 100% high salt buffer. Peak fractions were pooled, mixed with TEV protease, and dialyzed overnight in 7 kDa MWCO SnakeSkin dialysis tubing (Thermo Scientific) against low salt buffer. The protein was then applied to a HiTrap SP HP (5 ml) column (Cytiva) equilibrated in low salt buffer. The column was washed with 10 CV of low salt buffer and the protein was eluted off the HiTrap SP HP column using a 20 CV linear gradient from 0% low salt buffer to 100% high salt buffer. Peak fractions were pooled and concentrated with 50 kDa MWCO Amicon Ultra Centrifugal Filters (Merck) and applied to a Superdex 200 Increase 10/300 GL (Cytiva) column equilibrated in 500 mM NaCl, 20 mM Na-HEPES pH 7.4, 10% (v/v) glycerol, and 1 mM TCEP. Fractions containing UVSSA were concentrated with 50 kDa MWCO Amicon Ultra Centrifugal Filters (Merck). Protein concentration was determined as described and UVSSA was aliquoted, flash-frozen, and stored at −80°C.

For *H. sapiens* CSA-DDB1, the filtered supernatant was applied to a 5-ml HisTrap HP column (Cytiva) equilibrated in lysis buffer. The column was washed with 5 CV of Lysis buffer (400 mM NaCl, 20 mM Na-HEPES pH 7.4, 10% (v/v) glycerol, 30 mM imidazole pH 8.0, and 5 mM 2-mercaptoethanol, 0.284 μg ml−1 leupeptin, 1.37 μg ml−1 pepstatin A, 0.17 mg ml−1 PMSF, and 0.33 mg ml−1 benzamidine), followed by 20 CV of High Salt buffer (1 M NaCl, 20 mM Na-HEPES pH 7.4, 10% (v/v) glycerol, 30 mM imidazole pH 8.0, and 5 mM 2-mercaptoethanol, 0.284 μg ml−1 leupeptin, 1.37 μg ml−1 pepstatin A, 0.17 mg ml−1 PMSF, and 0.33 mg ml−1 benzamidine). The column was washed with 5 CV of Lysis buffer and 5 CV of low salt buffer (150 mM NaCl, 20 mM Na-HEPES pH 7.4, 10% (v/v) glycerol, 30 mM imidazole pH 8.0, and 5 mM 2-mercaptoethanol, 0.284 μg ml−1 leupeptin, 1.37 μg ml−1 pepstatin A, 0.17 mg ml−1 PMSF, and 0.33 mg ml−1 benzamidine). After washing, a HiTrap Q HP (5 ml) column equilibrated in low salt buffer was attached to the 5-ml HisTrap HP column. The protein was eluted onto the HiTrap Q HP with a 10 CV long step gradient of 100% Elution buffer (Lysis buffer supplemented with 500 mM imidazole). The HisTrap HP column was then removed and the HiTrap Q column was then washed with 5 CV of Low salt buffer. The protein was eluted off the HiTrap Q HP column using a 20 CV long linear gradient from 0% Low salt buffer to 100% High salt buffer. Peak fractions were pooled, mixed with TEV protease and dialysed overnight in 7 kDa MWCO SnakeSkin dialysis tubing (Thermo Scientific) against Dialysis buffer (400 mM NaCl, 20 mM Na-HEPES pH 7.4, 10% (v/v) glycerol, 50 mM imidazole pH 8.0, and 5 mM 2-mercaptoethanol, 0.284 μg ml−1 leupeptin, 1.37 μg ml−1 pepstatin A, 0.17 mg

ml−1 PMSF, and 0.33 mg ml−1 benzamidine). The flowthrough containing the complex was pooled and concentrated with 100 kDa MWCO Amicon Ultra Centrifugal Filters (Merck) and applied to a Superdex 200 Increase 10/300 GL (Cytiva) column equilibrated in 400 mM NaCl, 20 mM Na-HEPES pH 7.4, 10% (v/v) glycerol, and 1 mM TCEP. Fractions containing the complex were concentrated with 100 kDa MWCO Amicon Ultra Centrifugal Filters (Merck). Protein concentration was determined as described and CSA-DDB1 was aliquoted, flash-frozen, and stored at −80°C.

For *H. sapiens* DDA1, the filtered supernatant was applied to a 5-ml HisTrap HP column (Cytiva) equilibrated in lysis buffer (500 mM NaCl, 20 mM Na-HEPES pH 7.4, 10% (v/v) glycerol, 30 mM imidazole pH 8.0, and 5 mM 2-mercaptoethanol, 0.284 μg ml−1 leupeptin, 1.37 μg ml−1 pepstatin A, 0.17 mg ml−1 PMSF, and 0.33 mg ml−1 benzamidine). The column was washed with 5 CV of lysis buffer followed by 20 CV of high salt buffer, and 5 CV of lysis buffer. A self-packed XK column (Cytiva) with 15 mL of amylose resin (NEB) was attached to the HisTrap column which was then equilibrated into Lysis buffer. Sample was directly eluted onto the Amylose column with a 10 CV long step gradient of 100% elution buffer (lysis buffer supplemented with 500 mM imidazole). The HisTrap HP column was removed, and the amylose column was then washed with 5 CV of lysis buffer. The protein was eluted off the amylose column using an amylose elution buffer (lysis buffer supplemented with 116.9 mM maltose). Peak fractions were pooled, mixed with TEV protease and dialysed overnight in 7 kDa MWCO SnakeSkin dialysis tubing (Thermo Scientific) against lysis buffer (500 mM NaCl, 20 mM Na-HEPES pH 7.4, 10% (v/v) glycerol, 50 mM imidazole pH 8.0, and 5 mM 2-mercaptoethanol, 0.284 μg ml−1 leupeptin, 1.37 μg ml−1 pepstatin A, 0.17 mg ml−1 PMSF, and 0.33 mg ml−1 benzamidine). The dialyzed sample was subsequently applied to a 5 mL HisTrap column equilibrated in lysis buffer. The flow-through containing DDA1 was pooled and concentrated with 10 kDa MWCO Amicon Ultra Centrifugal Filters (Merck) and applied to a HiLoad 16/600 Superdex 75 (Cytiva) column equilibrated in 500 mM NaCl, 20 mM Na-HEPES pH 7.4, 10% (v/v) glycerol, and 1 mM TCEP. Fractions containing DDA1 were concentrated with 10 kDa MWCO Amicon Ultra Centrifugal Filters (Merck). Protein concentration was determined as described and DDA1 was aliquoted, flash-frozen, and stored at −80°C.

Complex preparation for cryo-EM—All concentrations refer to the final concentrations in the transcription reaction. RNA (5'–AUCGAGAGGA–3') and template DNA (5'– GAG GTC ACT CCA GTG AAT TCG AGC TCG CAA CAA TGA GCA CAT TCG CTC TGC TCC TTC TCC CAT CCT CTC GAT GGC TAT GAG ATC AAC TAG–3') were mixed and annealed as described.[14] 80 pmol nM of DNA·RNA hybrid were incubated with 80 pmol *S. scrofa* RNA polymerase II and incubated for 10 min on ice. 1040 pmol non-template DNA (5'–CTA GTT GAT CTC ATA TTT CAT TCC TAC TCA GGA GAA GGA GCA GAG CGA ATG TGC TCA TTG TTG CGA GCT CGA ATT CAC TGG AGT GAC CTC–3') was added to the mixture and again incubated for 10 min on ice. A factor mix was prepared separately with 2400 pmol each of UVSSA, CSB, and CSA-DDB1, as well as 3200 pmol each of STK19, ELOF1, and DDA1. The factor mix was incubated for 10 min on ice. The factor mix was subsequently added to the elongation complex and incubated for 10 min on ice. ADP·BeF_3, water and compensation buffer were added to adjust to a final concentration

of buffer components of 330 mM NaCl, 20 mM Na·HEPES pH 7.4, 5 % (v/v) glycerol, 0.3 mM ADP·BeF_3, and 1 mM TCEP. The reaction was incubated for 10 min on ice. The sample was dialyzed for 3 hours into a final buffer of 100 mM NaCl, 20 mM HEPES, pH 7.4, 3 mM $MgCl_2$, 5% (v/v) glycerol, and 1 mM TCEP. The sample was centrifuged for 10 min at 21,300*g* and applied to a Superose 6 Increase 3.2/300 (Cytiva) on an Äkta pure 25 with Micro kit (Cytiva). 50 μL fractions were collected. Peak fraction samples were applied to NuPAGE 4–12% Bis-Tris gels (Invitrogen) and run in 1X MES buffer for 30 min at 200 V to assess complex formation. The gel was stained with One-Step Blue Protein Gel Stain (Biotum) and imaged. Relevant peak fractions were individually crosslinked with 0.1% (v/v) glutaraldehyde for 10 min on ice and then quenched with 8 mM aspartate and 2 mM lysine for 10 min on ice. The reactions were transferred to a Slide-A-Lyzer Mini Dialysis Unit 20 K MWCO (Thermo Scientific) and dialyzed against a buffer containing 100 mM NaCl, 20 mM Na-HEPES pH 7.4, and 1 mM TCEP for 3 h at 4°C.

Complex concentrations were quantified by absorbance at 280 nm. The molar extinction coefficient of the complex was obtained by summing the molar extinction coefficient of all individual components. The fraction with the nominal highest concentration (~600 nM) was selected for analysis by cryo-EM. Quantifoil UltrAufoil R 2/2, 200 Mesh, Au grids were glow discharged for 120 s at 30 mA and 0.38 mBar with 10 s hold time at 0.38 mBar using a Pelco Easiglow plasma discharge system. 2 μL of sample were applied on each side of the grid, incubated for 10 s, blotted with Ted Pella standard Vitrobot filter paper for 3 s with blot force 8 and vitrified by plunging into liquid ethane using a Vitrobot Mark IV (FEI Company), operated at 4°C and 100% humidity. Sample application from both sites and sample incubation for 8 s has consistently resulted in better ice quality for transcription elongation complexes compared to single-sided sample application.

Cryo-electron microscopy and image processing—Cryo-EM data were collected on a ThermoFisher Scientific Titan Krios operated at 300 keV equipped with a Falcon 4 and a Selectris energy filter. Data acquisition was automated using EPU at a nominal magnification of 130,000x, corresponding to a pixel size of 0.94 Å in nanoprobe EFTEM mode. Movies consisting of 63 frames were collected in counted mode with an exposure time of 5.53 s. The electron flux was 9.48 e^- $Å^{-2}$ s^{-1} with a total dose of 52.4 e^- $Å^{-2}$. Image processing and analysis were performed with cryoSPARC (version 4.4.1) using default parameters, unless stated otherwise.

Movies were aligned using patch motion correction followed by contrast transfer function (CTF) estimation in cryoSPARC. Particles were picked by blob-based automatic picking, resulting in 3,742,711 particles from 15,521 micrographs. Particles were extracted with a Fourier binned box size of 300 pixels (pixel size of 1.47 Å). All classifications and refinements were conducted in cryoSPARC. Volumes employed for masking of areas of interest were generated by low-pass filtering the regions of interest to 10–15 Å and then using cryoSPARC to expand the volume containing the area of interest by 1–3 hard pixels and 3–7 soft pixels.

Three *ab initio* models were generated from a subset of 20,000 particles. The *ab initio* models were then used to select for particles that contain RNA polymerase II and TC-NER

factors via heterogeneous refinements and 3D classification, resulting in a subset of about 1,391,445 particles. The selected particles were subsequently 3D classified to remove low-resolution particles. A non-uniform refinement was performed, and the particles (1,123,600 particles) were recentered and re-extracted (box size of 468 pixels with a pixel size of 0.94 Å). The re-extracted particles were refined. Local and global CTF refinement and reference-based motion correction was completed. The subsequent refined particles were further classified using 3D classification to improve occupancy of DDB1 and Pol II subunits. Particle duplicates were removed, and the particles were again refined.

Subsequent local CTF refinement and non-homogeneous refinement resulted in the 1.9 Å reconstruction of the TC-NER complex with STK19 and DDA1 (map i), close to the nominal Nyquist frequency of 1.88 Å. Refinements of diverse areas of the map were performed including local refinements of the TC-NER factors (map ii), CSB (map iii), STK19 (map iv), DDB1-DDA1 (map v), and UVSSA-DDB1-DDA1 (map vi), RPB4/7 (map vii), and a 3D classification and subsequent local refinement for DDA1 (map viii). With help of an initial model of the complex, a composite map (map ix) of map i, iii, iv, vii, and viii was generated using PHENIX (version 1.20.1).

Model building and refinement—Structures of the TC-NER complex with ELOF1 (PDB ID 8B3D), were rigid body docked into the overall map. AlphaFold-Multimer structures corresponding to CSA-CSB, DDB1-CSA-UVSSA, CSB, STK19, DDA1-DDB1, and STK19-RPB1 predictions were superposed onto the initial TC-NER structure and used to further built/replace chains of the initial model to complete the structure of the TC-NER complex with STK19 and DDA1. Density in the active site of Pol II allowed unambiguous assignment of the DNA register by defining purine and pyrimidine bases in the DNA·RNA hybrid. Identification of the register was conducted in map i. We additionally observed two additional densities next to the metal A and docked water molecules into these densities. We note additional density for three amino acids bound to ATPase lobe 1 of CSB that we could not unambiguously assign. The atomic model was locally adjusted and refined using ISOLDE (version 1.7.1) with help of all local refinements. The overall atomic model was subsequently real space refined in PHENIX against map ix. Refinement statistics are reported in Table S2. Additional information on input structural models and model confidence is given in Table S3.

Figure generation—All structure figures were generated in UCSF ChimeraX. Angular distribution plots were generated using the available Warp tool. FSC curves were generated in cryoSPARC and adjusted in Adobe Illustrator.

QUANTIFICATION AND STATISTICAL ANALYSIS

Quantification of error-free repair—All quantified conditions were performed three or more times, except for Figures 2B, S1H, and S1I, which were performed twice. Gel images were quantified using ImageJ (NIH). First, the intensity values for the larger repaired DNA product and the remaining undamaged DNA fragment were quantified. Next, their intensities were normalized to size before the ratio of repaired and undamaged fragment was calculated to determine the percentage of error-free repair. These values were plotted in GraphPad

Prism v.10.2.2, as shown in Figure 1E with error bars representing the standard deviation from the mean (the relevant details are also listed in the figure legend). To determine the relative error-free repair at 120 min plotted in Figure 1F, the percentage of "repaired" DNA at 0 min (i.e. undamaged plasmid in the input sample; see lane 1 in Figure 1D) was first subtracted from the percentage of error-free repair at 120 min for all conditions. Next, to calculate repair relative to condition I (which was given a value of 1), all adjusted values at 120 min were divided by the value in condition I. This analysis was performed for each independent experiment, and data for all replicates was plotted together, showing individual data points as circles and the average value as a bar.

Relative TC-NER activities at 120 min in Figure 2A and all subsequent TC-NER assays were calculated by first determining the percentage of error-free repair as described above. Next, instead of subtracting the 0 min input value, the 120 min value of each condition I (no repair factor or all but one TC-NER factor present) was subtracted from all other conditions. In each independent experiment, repair relative to condition II (all wild-type TC-NER factors present; given the value 1) was calculated by dividing values of all conditions by the value of condition II. Data points from independent assays were plotted together in GraphPad Prism v.10.2.2, as described above.

Supplementary Material

Refer to Web version on PubMed Central for supplementary material.

ACKNOWLEDGEMENTS

We are grateful to Stephen Buratowski and members of his group for providing numerous reagents and for many helpful discussions, which were instrumental in helping us develop cell-free transcription. We thank Daniel Durocher and Dheva Setiaputra for alerting us to the predicted interaction between STK19 and CSA. Thanks to Seychelle Vos, Karen Adelman, Maria Jessica Bruzzone and members of the Walter laboratory for feedback on the manuscript and to Martijn Luijsterburg and Jesper Svejstrup for communicating results before publication. We thank the Harvard Cryo-EM Center for Structural Biology at Harvard Medical School for support with data collection. T.E.T.M. was supported by an HHMI fellowship of The Jane Coffin Childs Memorial Fund for Medical Research and an EMBO Long-term fellowship (ALTF 1316-2016). L.F. is supported by the NIH Director's New Innovator Award (DP2-ES036404). This work was supported by NIH grant HL098316 to J.C.W., who is a Howard Hughes Medical Institute Investigator and an American Cancer Society Research Professor.

REFERENCES

1. Schärer OD (2013). Nucleotide Excision Repair in Eukaryotes. Cold Spring Harb. Perspect. Biol. 5, a012609. 10.1101/cshperspect.a012609.
2. Lans H, Hoeijmakers JHJ, Vermeulen W, and Marteijn JA (2019). The DNA damage response to transcription stress. Nat Rev Mol Cell Bio 20, 766–784. 10.1038/s41580-019-0169-4. [PubMed: 31558824]
3. Jia N, Guo C, Nakazawa Y, Heuvel D. van den, Luijsterburg MS, and Ogi T. (2021). Dealing with transcription-blocking DNA damage: Repair mechanisms, RNA polymerase II processing and human disorders. Dna Repair 106, 103192. 10.1016/j.dnarep.2021.103192.
4. Moreno NN, Olthof AM, and Svejstrup JQ (2023). Transcription-Coupled Nucleotide Excision Repair and the Transcriptional Response to UV-Induced DNA Damage. Annu. Rev. Biochem 92, 81–113. 10.1146/annurev-biochem-052621-091205. [PubMed: 37040775]
5. Selby CP, Lindsey-Boltz LA, Li W, and Sancar A. (2023). Molecular Mechanisms of Transcription-Coupled Repair. Annu. Rev. Biochem 92, 115–144. 10.1146/annurev-biochem-041522-034232. [PubMed: 37001137]

6. Tsutakawa SE, Tsai C-L, Yan C, Bralić A, Chazin WJ, Hamdan SM, Schärer OD, Ivanov I, and Tainer JA (2020). Envisioning how the prototypic molecular machine TFIIH functions in transcription initiation and DNA repair. Dna Repair 96, 102972. 10.1016/j.dnarep.2020.102972.
7. Aboussekhra A, Biggerstaff M, Shivji MKK, Vilpo JA, Moncollin V, Podust VN, Protić M, Hübscher U, Egly J-M, and Wood RD (1995). Mammalian DNA nucleotide excision repair reconstituted with purified protein components. Cell 80, 859–868. 10.1016/0092-8674(95)90289-9. [PubMed: 7697716]
8. Mu D, Park C-H, Matsunaga T, Hsu DS, Reardon JT, and Sancar A. (1995). Reconstitution of Human DNA Repair Excision Nuclease in a Highly Defined System (*). J. Biol. Chem 270, 2415–2418. 10.1074/jbc.270.6.2415. [PubMed: 7852297]
9. Bohr VA, Smith CA, Okumoto DS, and Hanawalt PC (1985). DNA repair in an active gene: Removal of pyrimidine dimers from the DHFR gene of CHO cells is much more efficient than in the genome overall. Cell 40, 359–369. 10.1016/0092-8674(85)90150-3. [PubMed: 3838150]
10. Mellon I, Spivak G, and Hanawalt PC (1987). Selective removal of transcription-blocking DNA damage from the transcribed strand of the mammalian DHFR gene. Cell 51, 241–249. 10.1016/0092-8674(87)90151-6. [PubMed: 3664636]
11. Hanawalt PC (1994). Transcription-Coupled Repair and Human Disease. Science 266, 1957–1958. 10.1126/science.7801121. [PubMed: 7801121]
12. Heuvel D. van den, Weegen van der Y, Boer DEC., Ogi T, and Luijsterburg MS. (2021). Transcription-Coupled DNA Repair: From Mechanism to Human Disorder. Trends Cell Biol 31, 359–371. 10.1016/j.tcb.2021.02.007. [PubMed: 33685798]
13. Xu J, Lahiri I, Wang W, Wier A, Cianfrocco MA, Chong J, Hare AA, Dervan PB, DiMaio F, Leschziner AE, et al. (2017). Structural Basis for Eukaryotic Transcription-Coupled DNA Repair Initiation. Nature 551, 653–657. 10.1038/nature24658. [PubMed: 29168508]
14. Kokic G, Wagner FR, Chernev A, Urlaub H, and Cramer P. (2021). Structural basis of human transcription–DNA repair coupling. Nature 598, 368–372. 10.1038/s41586-021-03906-4. [PubMed: 34526721]
15. Weegen Y. van der, Golan-Berman H, Mevissen TET, Apelt K, González-Prieto R, Goedhart J, Heilbrun EE, Vertegaal ACO, Heuvel van den D, Walter JC, et al. (2020). The cooperative action of CSB, CSA, and UVSSA target TFIIH to DNA damage-stalled RNA polymerase II. Nat Commun 11, 2104. 10.1038/s41467-020-15903-8. [PubMed: 32355176]
16. Nakazawa Y, Hara Y, Oka Y, Komine O, Heuvel D. van den, Guo C, Daigaku Y, Isono M, He Y, Shimada M, et al. (2020). Ubiquitination of DNA Damage-Stalled RNAPII Promotes Transcription-Coupled Repair. Cell 180, 1228–1244.e24. 10.1016/j.cell.2020.02.010. [PubMed: 32142649]
17. Weegen Y. van der, Lint K. de, Heuvel D. van den, Nakazawa Y, Mevissen TET, Schie JJM van, Alonso MSM, Boer DEC, González-Prieto R, Narayanan IV, et al. (2021). ELOF1 is a transcription-coupled DNA repair factor that directs RNA polymerase II ubiquitylation. Nat Cell Biol 23, 595–607. 10.1038/s41556-021-00688-9. [PubMed: 34108663]
18. Geijer ME, Zhou D, Selvam K, Steurer B, Mukherjee C, Evers B, Cugusi S, Toorn M. van, Woude M. van der, Janssens RC, et al. (2021). Elongation factor ELOF1 drives transcription-coupled repair and prevents genome instability. Nat Cell Biol 23, 608–619. 10.1038/s41556-021-00692-z. [PubMed: 34108662]
19. Kokic G, Yakoub G, Heuvel D. van den, Wondergem AP, Meer PJ van der, Weegen Y. van der, Chernev A, Fianu I, Fokkens TJ, Lorenz S, et al. (2024). Structural basis for RNA polymerase II ubiquitylation and inactivation in transcription-coupled repair. Nat. Struct. Mol. Biol 31, 536–547. 10.1038/s41594-023-01207-0. [PubMed: 38316879]
20. Schwertman P, Lagarou A, Dekkers DHW, Raams A, Hoek AC van der, Laffeber C, Hoeijmakers JHJ, Demmers JAA, Fousteri M., Vermeulen W, et al. (2012). UV-sensitive syndrome protein UVSSA recruits USP7 to regulate transcription-coupled repair. Nat Genet 44, 598–602. 10.1038/ng.2230. [PubMed: 22466611]
21. Nakazawa Y, Sasaki K, Mitsutake N, Matsuse M, Shimada M, Nardo T, Takahashi Y, Ohyama K, Ito K, Mishima H, et al. (2012). Mutations in UVSSA cause UV-sensitive syndrome and impair RNA polymerase IIo processing in transcription-coupled nucleotide-excision repair. Nat Genet 44, 586–592. 10.1038/ng.2229. [PubMed: 22466610]

22. Zhang X, Horibata K, Saijo M, Ishigami C, Ukai A, Kanno S, Tahara H, Neilan EG, Honma M, Nohmi T, et al. (2012). Mutations in UVSSA cause UV-sensitive syndrome and destabilize ERCC6 in transcription-coupled DNA repair. Nat Genet 44, 593–597. 10.1038/ng.2228. [PubMed: 22466612]

23. Fei J, and Chen J. (2012). KIAA1530 Protein Is Recruited by Cockayne Syndrome Complementation Group Protein A (CSA) to Participate in Transcription-coupled Repair (TCR). J Biol Chem 287, 35118–35126. 10.1074/jbc.m112.398131. [PubMed: 22902626]

24. Okuda M, Nakazawa Y, Guo C, Ogi T, and Nishimura Y. (2017). Common TFIIH recruitment mechanism in global genome and transcription-coupled repair subpathways. Nucleic Acids Res 45, 13043–13055. 10.1093/nar/gkx970. [PubMed: 29069470]

25. Boeing S, Williamson L, Encheva V, Gori I, Saunders RE, Instrell R, Aygün O, Rodriguez-Martinez M, Weems JC, Kelly GP, et al. (2016). Multiomic Analysis of the UV-Induced DNA Damage Response. Cell Reports 15, 1597–1610. 10.1016/j.celrep.2016.04.047. [PubMed: 27184836]

26. Olivieri M, Cho T, Álvarez-Quilón A, Li K, Schellenberg MJ, Zimmermann M, Hustedt N, Rossi SE, Adam S, Melo H, et al. (2020). A Genetic Map of the Response to DNA Damage in Human Cells. Cell 182, 481–496.e21. 10.1016/j.cell.2020.05.040. [PubMed: 32649862]

27. Li Y, Gong Y, Zhou Y, Xiao Y, Huang W, Zhou Q, Tu Y, Zhao Y, Zhang S, Dai L, et al. (2024). STK19 is a DNA/RNA-binding protein critical for DNA damage repair and cell proliferation. J. Cell Biol 223, e202301090. 10.1083/jcb.202301090.

28. Rodríguez-Martínez M, Boissiére T, Gonzalez MN, Litchfield K, Mitter R, Walker J, Kjœr S, Ismail M, Downward J, Swanton C, et al. (2020). Evidence That STK19 Is Not an NRAS-dependent Melanoma Driver. Cell 181, 1395–1405.e11. 10.1016/j.cell.2020.04.014. [PubMed: 32531245]

29. Li J, Ma X, Wang X, Hu X, Fang S, Jin G, Liu K, and Dong Z. (2024). Mutations found in cancer patients compromise DNA binding of the winged helix protein STK19. Sci. Rep 14, 14098. 10.1038/s41598-024-64840-9. [PubMed: 38890355]

30. Lainé J, and Egly J. (2006). Initiation of DNA repair mediated by a stalled RNA polymerase IIO. Embo J 25, 387–397. 10.1038/sj.emboj.7600933. [PubMed: 16407975]

31. Sarsam RD, Xu J, Lahiri I, Gong W, Li Q, Oh J, Zhou Z, Hou P, Chong J, Hao N, et al. (2024). Elf1 promotes Rad26's interaction with lesion-arrested Pol II for transcription-coupled repair. Proc. Natl. Acad. Sci 121, e2314245121. 10.1073/pnas.2314245121.

32. Shivji MKK, Grey SJ, Strausfeld UP, Wood RD, and Blow JJ (1994). Cip1 inhibits DNA replication but not PCNA-dependent nucleotide excision—repair. Curr. Biol 4, 1062–1068. 10.1016/s0960-9822(00)00244-x. [PubMed: 7704570]

33. Hoogenboom WS, Douwel DK, and Knipscheer P. (2017). Xenopus egg extract: A powerful tool to study genome maintenance mechanisms. Dev. Biol 428, 300–309. 10.1016/j.ydbio.2017.03.033. [PubMed: 28427716]

34. Barrows JK, and Long DT (2019). Cell-free transcription in Xenopus egg extract. J Biol Chem 294, 19645–19654. 10.1074/jbc.ra119.011350. [PubMed: 31732562]

35. Wühr M, Freeman RM, Presler M, Horb ME, Peshkin L, Gygi SP, and Kirschner MW (2014). Deep proteomics of the Xenopus laevis egg using an mRNA-derived reference database. Current biology : CB 24, 1467–1475. 10.1016/j.cub.2014.05.044. [PubMed: 24954049]

36. Schmid EW, and Walter JC (2024). Predictomes: A classifier-curated database of AlphaFold-modeled protein-protein interactions. bioRxiv, 2024.04.09.588596. 10.1101/2024.04.09.588596.

37. Shabek N, Ruble J, Waston CJ, Garbutt KC, Hinds TR, Li T, and Zheng N. (2018). Structural insights into DDA1 function as a core component of the CRL4-DDB1 ubiquitin ligase. Cell Discov 4, 67. 10.1038/s41421-018-0064-8. [PubMed: 30564455]

38. Schiffmacher DAL, Lee S-H, Kliza KW, Theil AF, Akita M, Helfricht A, Bezstarosti K, Gonzalo-Hansen C, Attikum H. van, Vries MV, et al. (2024). The small CRL4CSA ubiquitin ligase component DDA1 regulates transcription-coupled repair dynamics. Nat. Commun 15, 6374. 10.1038/s41467-024-50584-7. [PubMed: 39075067]

39. Vidaković AT, Mitter R, Kelly GP, Neumann M, Harreman M, Rodríguez-Martínez M, Herlihy A, Weems JC, Boeing S, Encheva V, et al. (2020). Regulation of the RNAPII Pool Is Integral

to the DNA Damage Response. Cell 180, 1245–1261.e21. 10.1016/j.cell.2020.02.009. [PubMed: 32142654]

40. Kokic G, Chernev A, Tegunov D, Dienemann C, Urlaub H, and Cramer P. (2019). Structural basis of TFIIH activation for nucleotide excision repair. Nat Commun 10, 2885. 10.1038/s41467-019-10745-5. [PubMed: 31253769]
41. van den Heuvel et al., in this issue
42. Kim J, Li C-L, Chen X, Cui Y, Golebiowski FM, Wang H, Hanaoka F, Sugasawa K, and Yang W. (2023). Lesion recognition by XPC, TFIIH and XPA in DNA excision repair. Nature 617, 170–175. 10.1038/s41586-023-05959-z. [PubMed: 37076618]
43. Li C-L, Golebiowski FM, Onishi Y, Samara NL, Sugasawa K, and Yang W. (2015). Tripartite DNA Lesion Recognition and Verification by XPC, TFIIH, and XPA in Nucleotide Excision Repair. Mol Cell 59, 1025–1034. 10.1016/j.molcel.2015.08.012. [PubMed: 26384665]
44. Aibara S, Schilbach S, and Cramer P. (2021). Structures of mammalian RNA polymerase II pre-initiation complexes. Nature 594, 124–128. 10.1038/s41586-021-03554-8. [PubMed: 33902107]
45. He Y, Yan C, Fang J, Inouye C, Tjian R, Ivanov I, and Nogales E. (2016). Near-atomic resolution visualization of human transcription promoter opening. Nature 533, 359–365. 10.1038/nature17970. [PubMed: 27193682]
46. Faber J, and Nieuwkoop PD (1994). Normal Table of Xenopus Laevis (Daudin) (Garland Pub., New York) 10.1201/9781003064565.
47. Slenn TJ, Morris B, Havens CG, Freeman RM, Takahashi TS, and Walter JC (2014). Thymine DNA Glycosylase Is a CRL4Cdt2 Substrate*. J. Biol. Chem 289, 23043–23055. 10.1074/jbc.m114.574194. [PubMed: 24947512]
48. Yariv B, Yariv E, Kessel A, Masrati G, Chorin AB, Martz E, Mayrose I, Pupko T, and Ben-Tal N. (2023). Using evolutionary data to make sense of macromolecules with a “face-lifted” ConSurf. Protein Sci. 32, e4582. 10.1002/pro.4582. [PubMed: 36718848]
49. Heubes S, and Stemmann O. (2007). The AAA-ATPase p97-Ufd1-Npl4 is required for ERAD but not for spindle disassembly in Xenopus egg extracts. J Cell Sci 120, 1325–1329. 10.1242/jcs.006924. [PubMed: 17374636]
50. Matsuda T, and Cepko CL (2004). Electroporation and RNA interference in the rodent retina in vivo and in vitro. Proc. Natl. Acad. Sci 101, 16–22. 10.1073/pnas.2235688100. [PubMed: 14603031]
51. Gradia SD, Ishida JP, Tsai M-S, Jeans C, Tainer JA, and Fuss JO (2017). MacroBac: New Technologies for Robust and Efficient Large-Scale Production of Recombinant Multiprotein Complexes. Methods Enzymol 592, 1–26. 10.1016/bs.mie.2017.03.008. [PubMed: 28668116]
52. Schindelin J, Arganda-Carreras I, Frise E, Kaynig V, Longair M, Pietzsch T, Preibisch S, Rueden C, Saalfeld S, Schmid B, et al. (2012). Fiji: an open-source platform for biological-image analysis. Nat. Methods 9, 676–682. 10.1038/nmeth.2019. [PubMed: 22743772]
53. Punjani A, Rubinstein JL, Fleet DJ, and Brubaker MA (2017). cryoSPARC: algorithms for rapid unsupervised cryo-EM structure determination. Nat. Methods 14, 290–296. 10.1038/nmeth.4169. [PubMed: 28165473]
54. Liebschner D, Afonine PV, Baker ML, Bunkóczi G, Chen VB, Croll TI, Hintze B, Hung L-W, Jain S, McCoy AJ, et al. (2019). Macromolecular structure determination using X-rays, neutrons and electrons: recent developments in Phenix. Acta Crystallogr. Sect. D 75, 861–877. 10.1107/s2059798319011471.
55. Croll TI (2018). ISOLDE: a physically realistic environment for model building into low-resolution electron-density maps. Acta Crystallogr. Sect. D 74, 519–530. 10.1107/s2059798318002425.
56. Goddard TD, Huang CC, Meng EC, Pettersen EF, Couch GS, Morris JH, and Ferrin TE (2018). UCSF ChimeraX: Meeting modern challenges in visualization and analysis. Protein Sci. 27, 14–25. 10.1002/pro.3235. [PubMed: 28710774]
57. Juven-Gershon T, Cheng S, and Kadonaga JT (2006). Rational design of a super core promoter that enhances gene expression. Nat Methods 3, 917–922. 10.1038/nmeth937. [PubMed: 17124735]
58. Enoiu M, Jiricny J, and Schärer OD (2012). Repair of cisplatin-induced DNA interstrand crosslinks by a replication-independent pathway involving transcription-coupled repair and translesion synthesis. Nucleic Acids Res 40, 8953–8964. 10.1093/nar/gks670. [PubMed: 22810206]

59. Sparks J, and Walter JC (2019). Extracts for Analysis of DNA Replication in a Nucleus-Free System. Cold Spring Harb Protoc 2019, pdb.prot097154. 10.1101/pdb.prot097154.

60. Evans R, O'Neill M, Pritzel A, Antropova N, Senior A, Green T, Žídek A, Bates R, Blackwell S, Yim J, et al. (2022). Protein complex prediction with AlphaFold-Multimer. bioRxiv, 2021.10.04.463034. 10.1101/2021.10.04.463034.

61. Mirdita M, Schütze K, Moriwaki Y, Heo L, Ovchinnikov S, and Steinegger M. (2022). ColabFold: making protein folding accessible to all. Nat Methods 19, 679–682. 10.1038/s41592-022-01488-1. [PubMed: 35637307]

62. Steinegger M, and Söding J. (2017). MMseqs2 enables sensitive protein sequence searching for the analysis of massive data sets. Nat. Biotechnol 35, 1026–1028. 10.1038/nbt.3988. [PubMed: 29035372]

63. Lim Y, Tamayo-Orrego L, Schmid E, Tarnauskaite Z, Kochenova OV, Gruar R, Muramatsu S, Lynch L, Schlie AV, Carroll PL, et al. (2023). In silico protein interaction screening uncovers DONSON's role in replication initiation. Science 381, eadi3448–eadi3448. 10.1126/science.adi3448.

64. Varadi M, Bertoni D, Magana P, Paramval U, Pidruchna I, Radhakrishnan M, Tsenkov M, Nair S, Mirdita M, Yeo J, et al. (2023). AlphaFold Protein Structure Database in 2024: providing structure coverage for over 214 million protein sequences. Nucleic Acids Res. 52, D368–D375. 10.1093/nar/gkad1011.

65. Bryant P, Pozzati G, and Elofsson A. (2022). Improved prediction of protein-protein interactions using AlphaFold2. Nat. Commun 13, 1265. 10.1038/s41467-022-28865-w. [PubMed: 35273146]

66. Farnung L, Vos SM, Wigge C, and Cramer P. (2017). Nucleosome-Chd1 structure and implications for chromatin remodelling. Nature 550, 539–542. 10.1038/nature24046. [PubMed: 29019976]

67. Vos SM, Farnung L, Urlaub H, and Cramer P. (2018). Structure of paused transcription complex Pol II-DSIF-NELF. Nature 560, 601–606. 10.1038/s41586-018-0442-2. [PubMed: 30135580]

HIGHLIGHTS

- Establishment of a cell-free system for vertebrate transcription-coupled DNA repair
- AlphaFold-Multimer screen predicts binding partners of STK19, including TFIIH
- Cryo-EM structure of STK19-containing TC-NER complex at 1.9 Å resolution
- STK19 couples RNA polymerase II stalling to downstream repair events

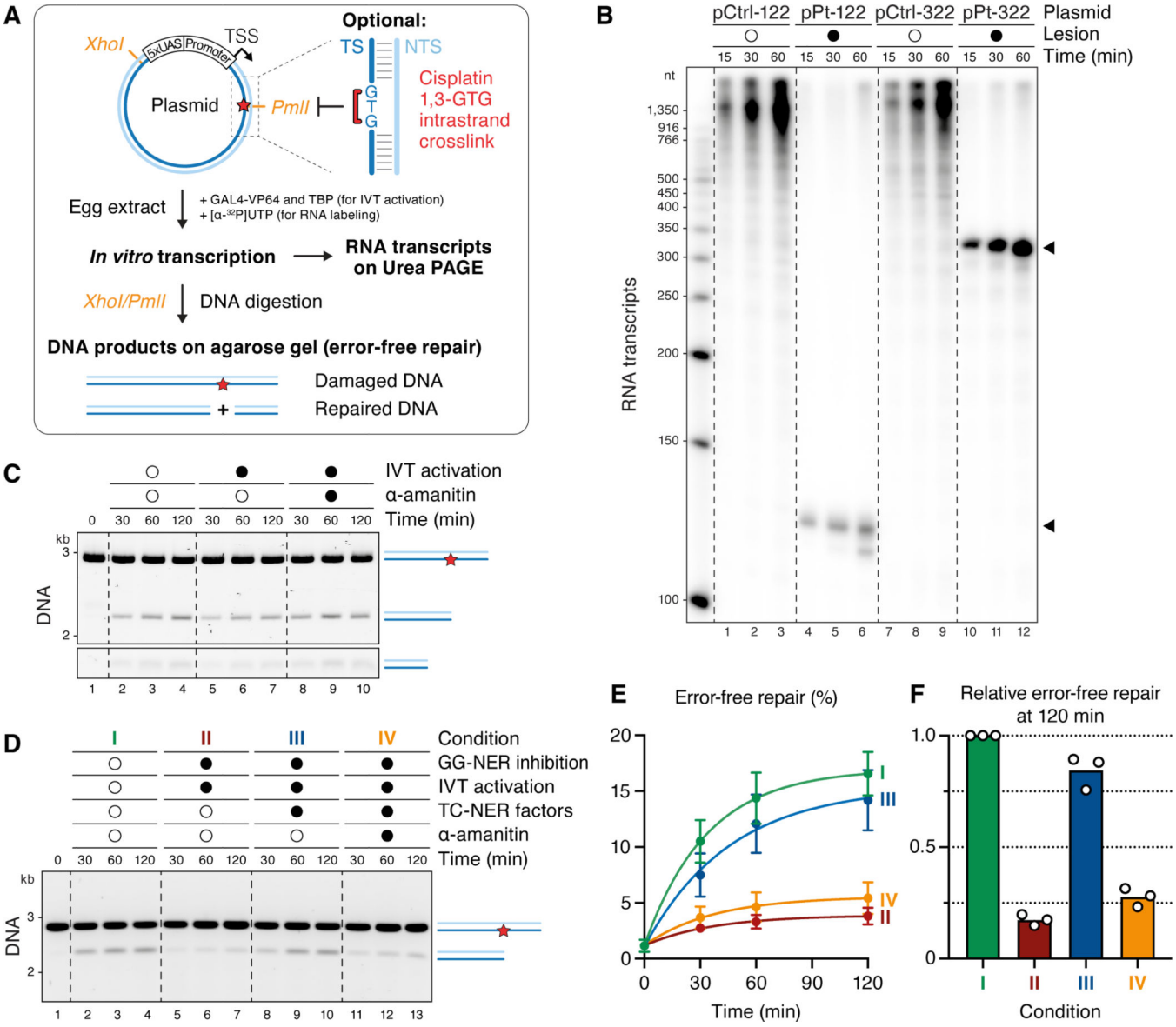

Figure 1. Transcription-coupled DNA repair in egg extracts

(A) Generic schematic of the plasmids used for *in vitro* transcription (IVT) and transcription-coupled DNA repair (including ones containing adenovirus major late and SCP2* promoters). The workflow for analyzing RNA transcripts and error-free DNA repair is outlined. UAS, upstream activation sequence; TSS, transcription start site; TS, template strand; NTS, non-template strand.

(B) Plasmids without (pCtrl) or with cisplatin 1,3-GTG intrastrand crosslinks (pPt) positioned 122 bp or 322 bp downstream of the TSS were added to NPE containing GAL4-VP64, TBP, and [α-^{32}P]UTP. At the indicated times, RNA was recovered, separated on a Urea-PAGE gel, and subjected to autoradiography. Open and closed circles indicate the absence or presence of a given condition (here the presence of a lesion), respectively. Arrows indicate transcripts of lesion-stalled Pol II.

(C) pPt-322 was incubated with NPE that was optionally supplemented with IVT activation mix (GAL4-VP64 and TBP) and α-amanitin (2 μM), as indicated (but not [α-^{32}P]UTP). DNA was recovered at indicated times, incubated with *XhoI* and *PmlI*, separated on an agarose gel, and visualized with SYBR Gold. Appearance of the 2.2 kb and 0.8 kb (bottom panel) restriction fragments indicates restoration of the *PmlI* site. A part of the gel without any bands has been removed. See Figure S1E for inhibitory effect of α-amanitin.

(D) Same assay as in (C) but using pPt-122. GG-NER was inhibited via addition of an inhibitory XPC antibody, transcription was induced, and the TC-NER cocktail was added, as indicated. The smaller (0.6 kb) fragment is not shown.

(E) Quantification of error-free repair of n = 3 experiments like the one shown in (D). To determine the percentage of repaired plasmids, the ratio of repaired to damaged DNA fragments in each lane was quantified (see Methods). Error bars represent the SD from the mean.

(F) Bar graph quantifying the error-free repair relative to condition I (GG-NER) at the 120 minute time point from (E), our standard approach to present the data throughout the paper. See also Figure S1.

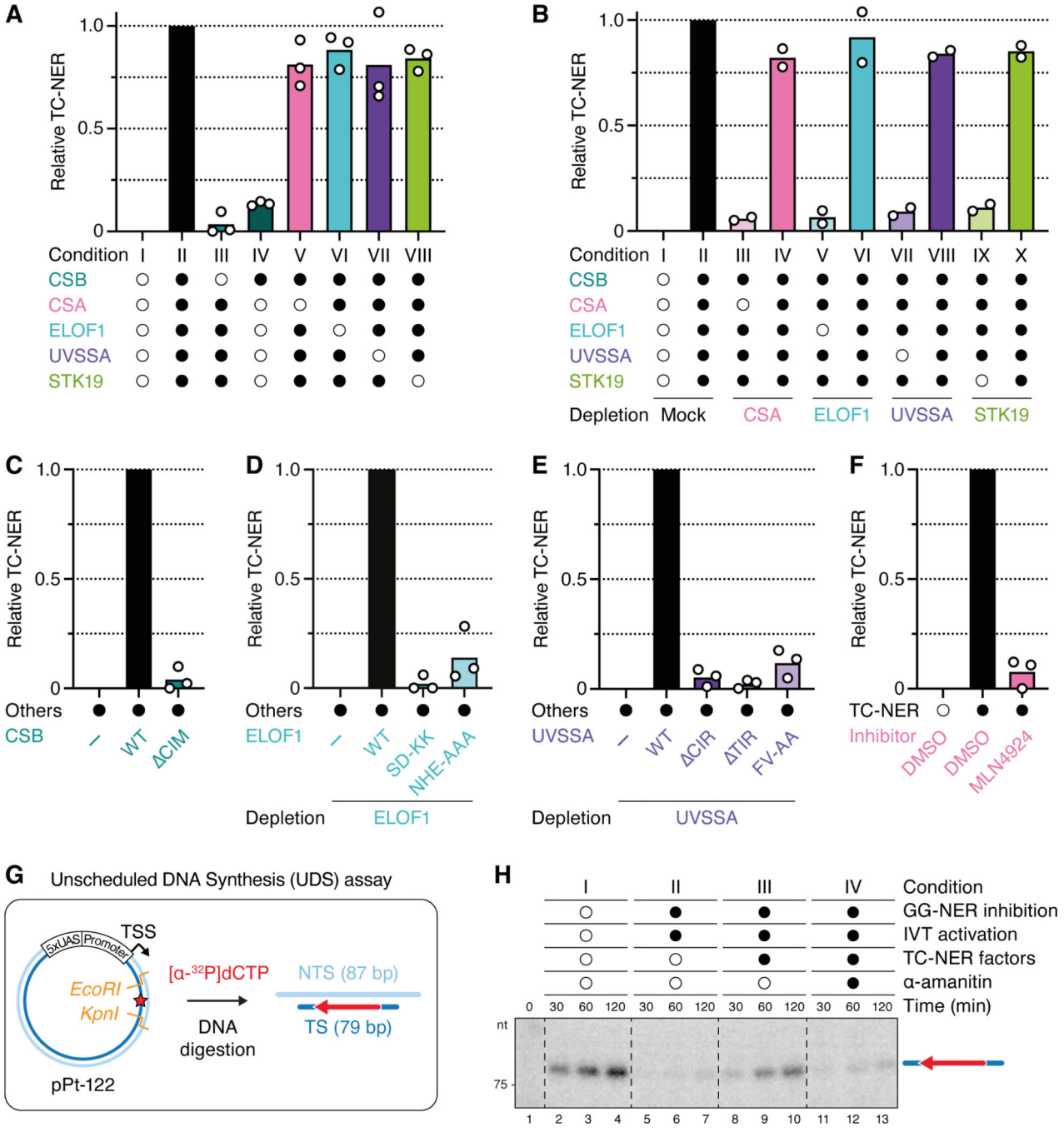

Figure 2. TC-NER in egg extracts requires known proteins, interactions, and STK19

(A) Error-free repair assay as described in Figures 1D and 1F, except that GG-NER was inhibited by immunodepletion of XPC from NPE. Open circles indicate factors that were omitted from the TC-NER cocktail. Data of three independent experiments for each condition is plotted. The quantified TC-NER activity for each condition is normalized to no repair in condition I and fully active repair in condition II, which are given values of 0 and 1, respectively. Condition II is the standard "TC-NER assay" used in all subsequent experiments. See Figures S2C-S2G for western blots of extracts used.

(B) TC-NER assay with NPE in which indicated proteins were immunodepleted. See Figures S2C-S2G for western blots of extracts used.
(C) TC-NER assay comparing recombinant human CSB variants. WT, wild-type; ΔCIM, amino acids 1385–1399 were deleted. See Figure S2H for western blot of extracts used.
(D) TC-NER assay in ELOF1-depleted NPE. Buffer or the indicated *X. laevis* ELOF1 variant was added. SD-KK, combination of S72K and D73K mutations to disrupt Pol II binding; NHE-AAA, combination of N30A, H31A, and E32A mutations to prevent CSA binding. See Figure S2I for western blot of extracts used.
(E) TC-NER assay in UVSSA-depleted NPE. Buffer or the indicated *X. laevis* UVSSA proteins expressed in wheat germ extract were added. ΔCIR, amino acids 99–201 were deleted, based on the analogous mutation that disrupts CSA binding in humans.[15] ΔTIR, deletion of residues 416–524; FV-AA, mutation of F425A and V428A to disrupt TFIIH binding. See Figure S2J for western blot of extracts used.
(F) TC-NER assay in NPE that was supplemented with DMSO or 200 μM MLN4924, which prevents cullin neddylation. See Figure S2K for western blot of extracts used.
(G) Schematic illustrating the gap filling assay. Staggered cutting by *EcoRI* and *KpnI* (orange lines) allowed resolution of the top (non-template) and bottom (template) strands.
(H) Unscheduled DNA Synthesis (UDS) assay. Repair reactions were performed as in Figure 1D, except that GG-NER was inhibited by XPC depletion, and that NPE was supplemented with [α-^{32}P]dCTP. DNA was recovered, digested with *EcoRI* and *KpnI*, separated on a Urea-PAGE gel, and subjected to autoradiography.
See also Figure S2.

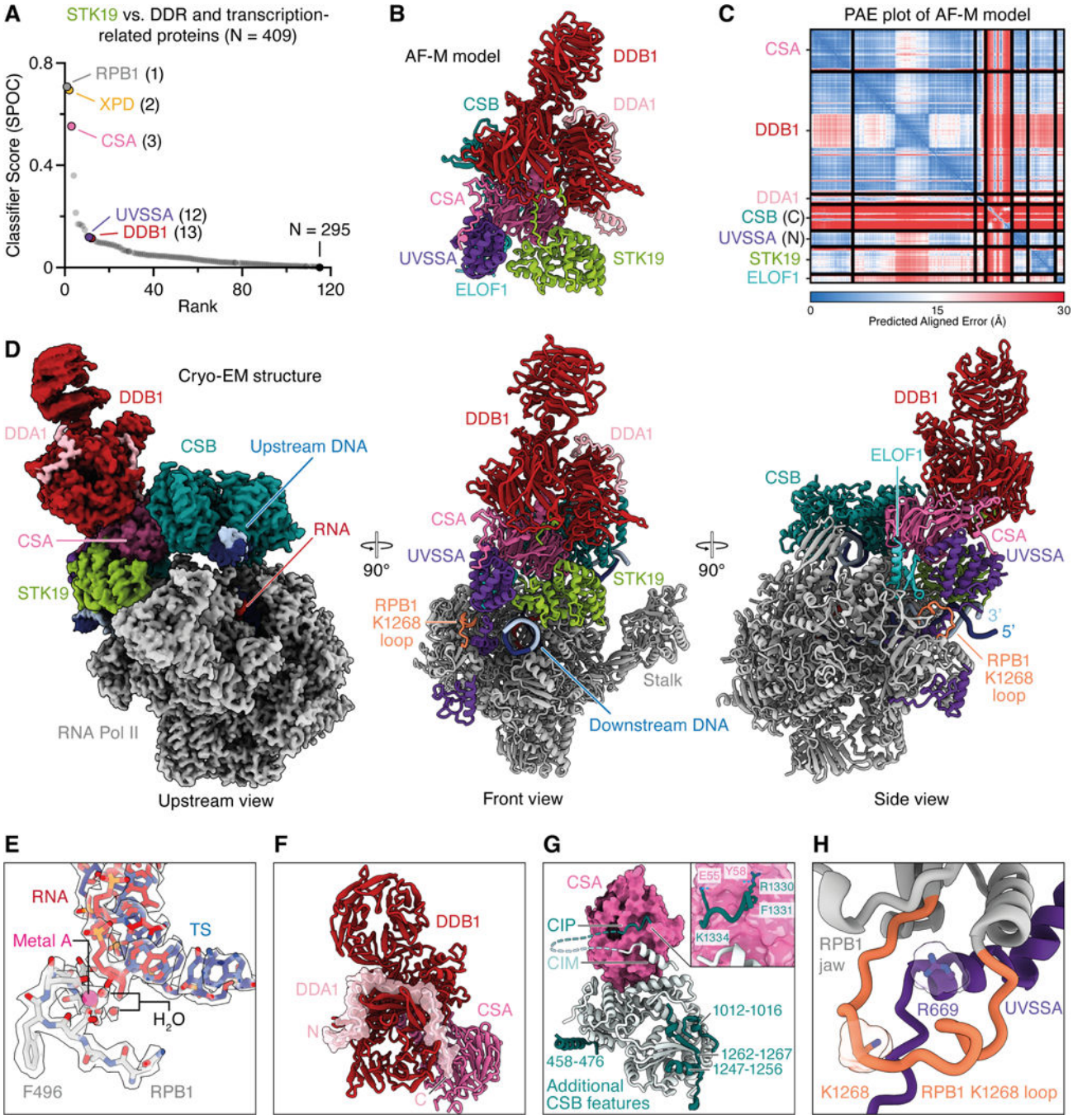

Figure 3. Structure of an STK19-containing TC-NER complex

(A) STK19 was "folded" with ~400 proteins using AlphaFold-Multimer (AF-M), and the resulting structure predictions were ranked by SPOC, a classifier trained to distinguish true from spurious AF-M predictions.

(B) Human CSA, DDB1, DDA1, CSB (aa 1250–1493), UVSSA (aa 1–150), STK19, and ELOF1 were folded in five models using AF-M, and a representative structure prediction is shown. The structure has confidence metrics: pLDDT = 82.7, PAE = 3.8, avg_models = 0.86.

(C) Representative predicted alignment error (PAE) plot for the AF-M model in (B).
(D) Three views of the STK19-containing TC-NER complex by cryo-EM. Structure is presented as a cartoon model (front and side views) or as the Coulomb potential (map xi; upstream view). Template strand, dark blue. Non-template strand, light blue. DDB1 β-propeller 2 is shown as low-pass filtered map (map i) superposed on map ix.
(E) Stick representation of Pol II active site. Coulomb potential map is shown as transparent volume. Metal A and two coordinating water molecules are clearly visible and shown as pink or red spheres, respectively.
(F) Interaction of DDB1, CSA, and DDA1. DDA1 is shown in surface and cartoon representation.
(G) New CSB features and interaction of CSA and CSB. CSA shown as surface, and CSB shown as cartoon model. Additional CSB features are colored in dark cyan. An N-terminal CSB α-helix (residues 458–476) binds to ATPase lobe 1, and a β-strand (residues 1262–1267) complements the β-sheet of ATPase lobe 2 in an anti-parallel orientation. The additional CSB β-strand is flanked by two α-helical elements (CSB residues 1012–1016 and 1247–1256). Inset, details of CSB's newly resolved CSA-interacting peptide (CIP) shown in cartoon representation with important side chains shown in stick representation.
(H) RPB1 K1268 loop shown with C-terminus of UVSSA. RPB1 K1268 contacts the start of the UVSSA C-terminus. UVSSA R669 inserts into the loop. UVSSA R669 and RPB1 K1268 residues are shown in stick and surface representation.
See also Figures S3-S6 and Tables S1-S3.

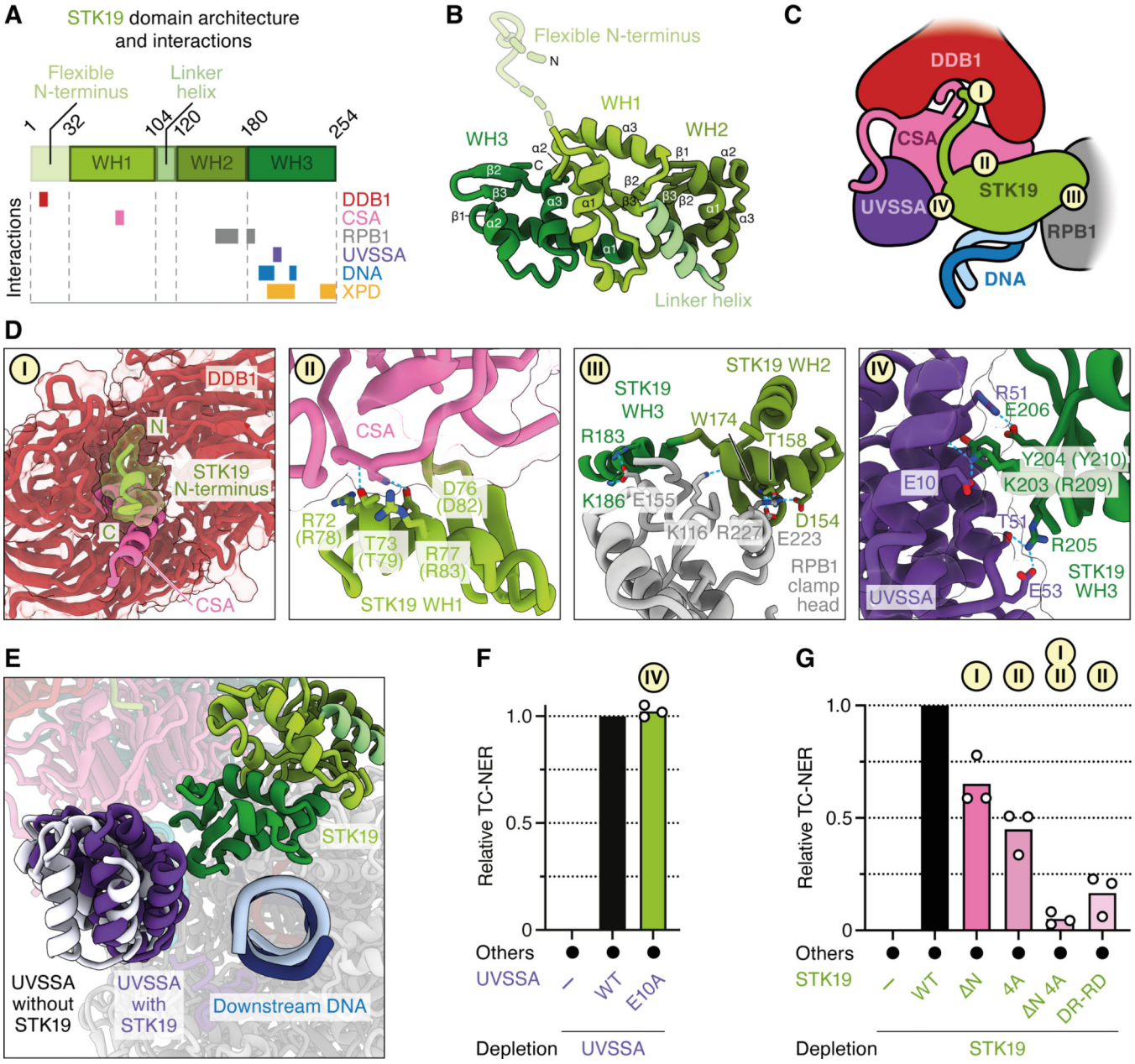

Figure 4. STK19 interacts with the TC-NER complex via CSA and DDB1

(A) Schematic showing the domain architecture of STK19 and interaction partners for each subdomain.

(B) Cryo-EM structure of STK19 colored by domain architecture. Unresolved residues are shown as dotted lines.

(C) Schematic showing STK19 and its interaction partners, including DNA.

(D) Close-up view of interaction sites I-IV from (C). STK19, UVSSA, and DDB1 are shown in cartoon and/or surface representation. CSA is shown as a cartoon model. STK19 N-terminal backbone could be resolved, amino acid register is not assigned. Residues forming hydrogen bonds at the interaction interfaces are shown in stick representation. Hydrogen bonds shown as dotted lines. *X. laevis* residues are shown in parentheses.

(E) Binding of STK19 to the TC-NER complex induces a shift of the UVSSA VHS domain towards the downstream DNA and STK19 by up to 8 Å. UVSSA VHS domain from TC-NER complex without STK19 shown in white (PDB ID 8B3D).
(F) TC-NER assay in UVSSA-depleted NPE. *X. laevis* UVSSA proteins expressed in wheat germ extract were added as indicated.
(G) TC-NER assay in STK19-depleted NPE. Buffer or the indicated recombinant *X. laevis* STK19 variants (Figure S2B) were added back. ΔN, deletion of amino acids 1–33; 4A, mutation of residues R78, T79, D82, and R83 to alanine; ΔN 4A, mutant containing both ΔN and 4A mutations; DR-RD, residues D82 and R83 were swapped.

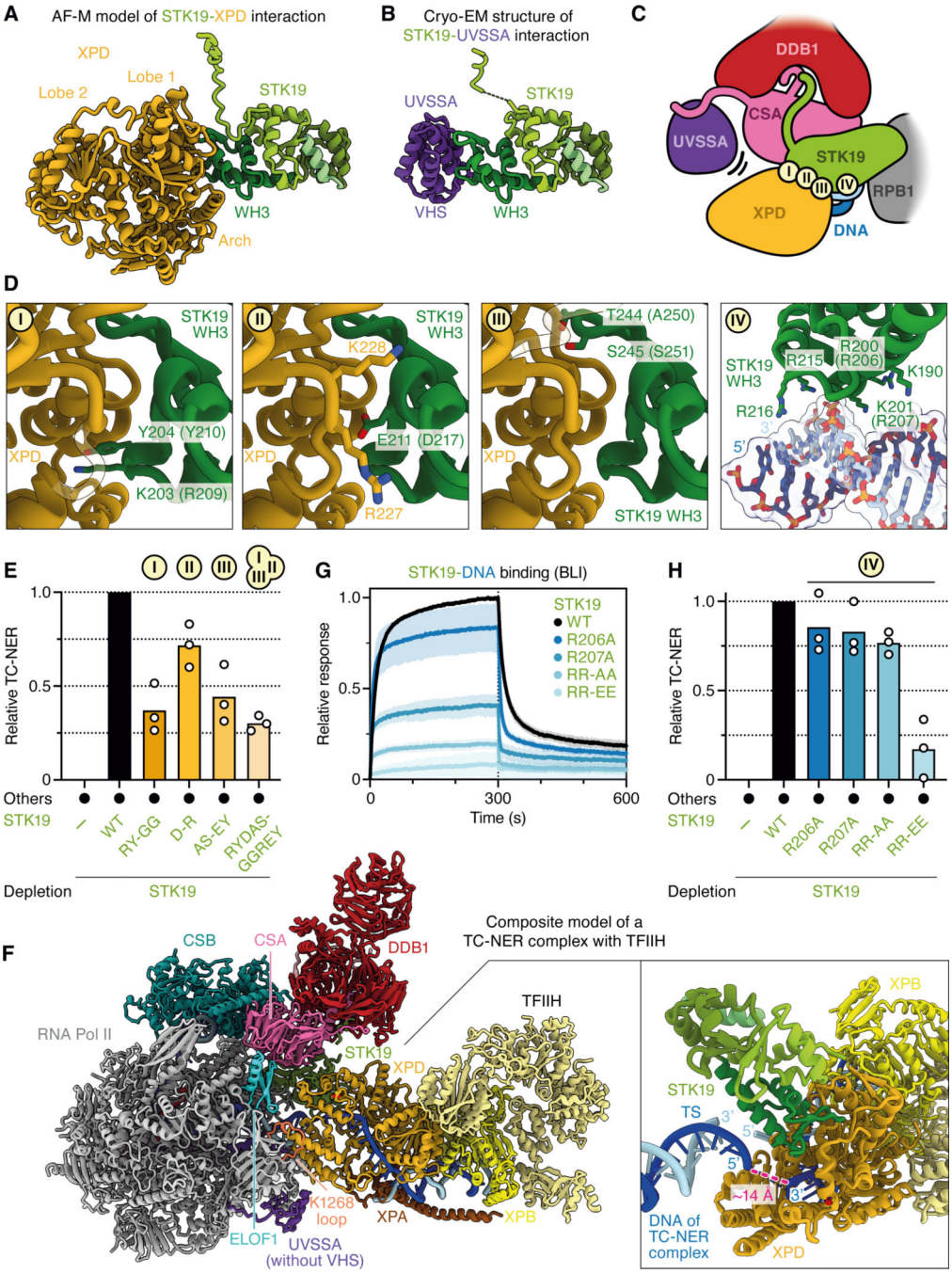

Figure 5. Mutations at the predicted STK19-XPD interface disrupt TC-NER, but STK19 DNA binding is not required

(A-B) AF-M prediction for STK19-XPD complex (A) and cryo-EM structure of STK19-UVSSA shown in Figure 3D (B). STK19 is depicted in the same orientation in both panels.

(C) Schematic showing STK19 and its interaction partners, including XPD. The proposed dissociation of UVSSA from CSA's β-propeller that allows XPD binding to STK19 is indicated.

(D) Close up view of interaction sites I-IV from (C). Amino acids shown in parentheses refer to *X. laevis*.

(E) TC-NER assay in STK19-depleted NPE. Buffer or the indicated purified *X. laevis* STK19 mutants (Figure S2B) were added back. RY-GG, mutation of R209 and Y210 within a loop in WH3 to glycine; D-R, D217R mutation; AS-EY, residues A250 (corresponding to T244 in *H. sapiens*) and S251 located in a loop within WH3 were mutated to larger residues to interfere with XPD recruitment; RYDAS-GGREY, combination of mutations in all three sites.

(F) Model for the positioning of TFIIH on the TC-NER complex mediated by STK19. The STK19-XPD AF-M model shown in (A) was aligned with STK19 in the cryo-EM TC-NER complex shown in Figure 3D. Subsequently, a TFIIH-XPA-DNA complex (PDB ID 6RO4) was aligned with XPD from the STK19-XPD structure prediction. The UVSSA VHS domain and CSA's C-terminal tail were removed for clarity and to reflect our model that the VHS domain moves to accommodate XPD. Inset, close-up of the STK19-XPD-DNA region. The distance between the template strand (TS) of the TC-NER complex and the ssDNA in XPD of the TFIIH complex is shown.

(G) Biolayer interferometry (BLI) assay measuring the interaction of *X. laevis* STK19 WT and the indicated mutants (Figure S2B) with a biotinylated 14 nt DNA duplex. RR-AA, combination of R206A and R207A; RR-EE, combination of R206E and R207E mutations. Data from at least three independent experiments per STK19 variant is plotted relative to STK19 WT. Error represents the SD from the mean.

(H) TC-NER assay in STK19-depleted NPE. Buffer or the indicated *X. laevis* STK19 mutants described in (G) were added back.

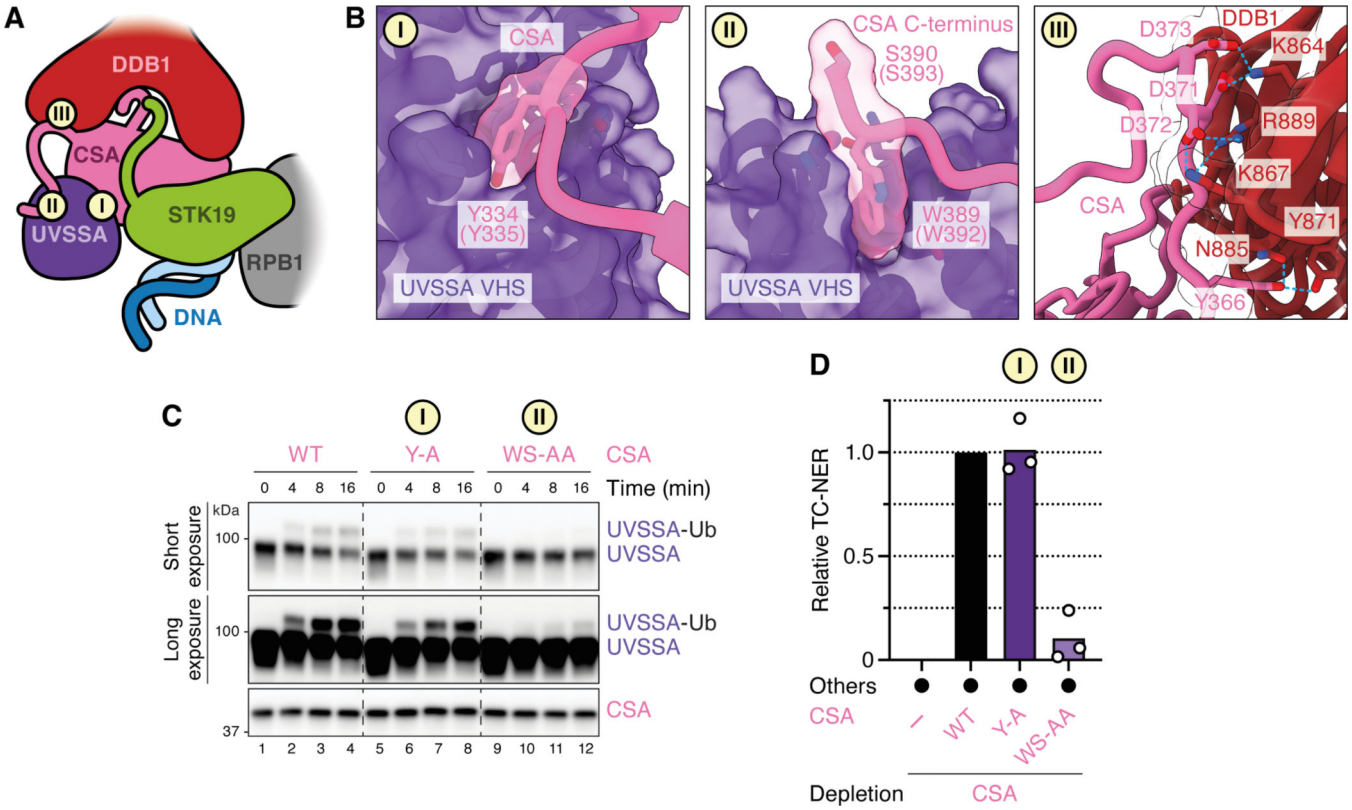

Figure 6. The C-terminus of CSA binds UVSSA and is essential for TC-NER

(A) Schematic showing that the VHS domain of UVSSA binds CSA at two points: (I) the CSA β-propeller and (II) the CSA C-terminal flexible tail (distal region). (III) Interaction of CSA's C-terminal tail (proximal region) with DDB1.

(B) Close up view of interaction sites I-III from (A). Amino acids shown in parentheses refer to *X. laevis*.

(C) *In vitro* ubiquitination assay. Recombinant *X. laevis* UVSSA was mixed with neddylated *X. laevis* $CRL4^{CSA}$ variants (WT, Y-A, or WS-AA; Figure S2B), ubiquitin, E1, UBE2E1, and ATP. At the indicated times, reaction products were immunoblotted for UVSSA and CSA. UVSSA-Ub, monoubiquitinated UVSSA. Y-A, Y335A mutation. WS-AA, combination of W392A and S393A mutations.

(D) TC-NER assay in CSA-depleted NPE. Buffer or the indicated *X. laevis* CSA mutants described in (C) were added back.

See also Figure S7.

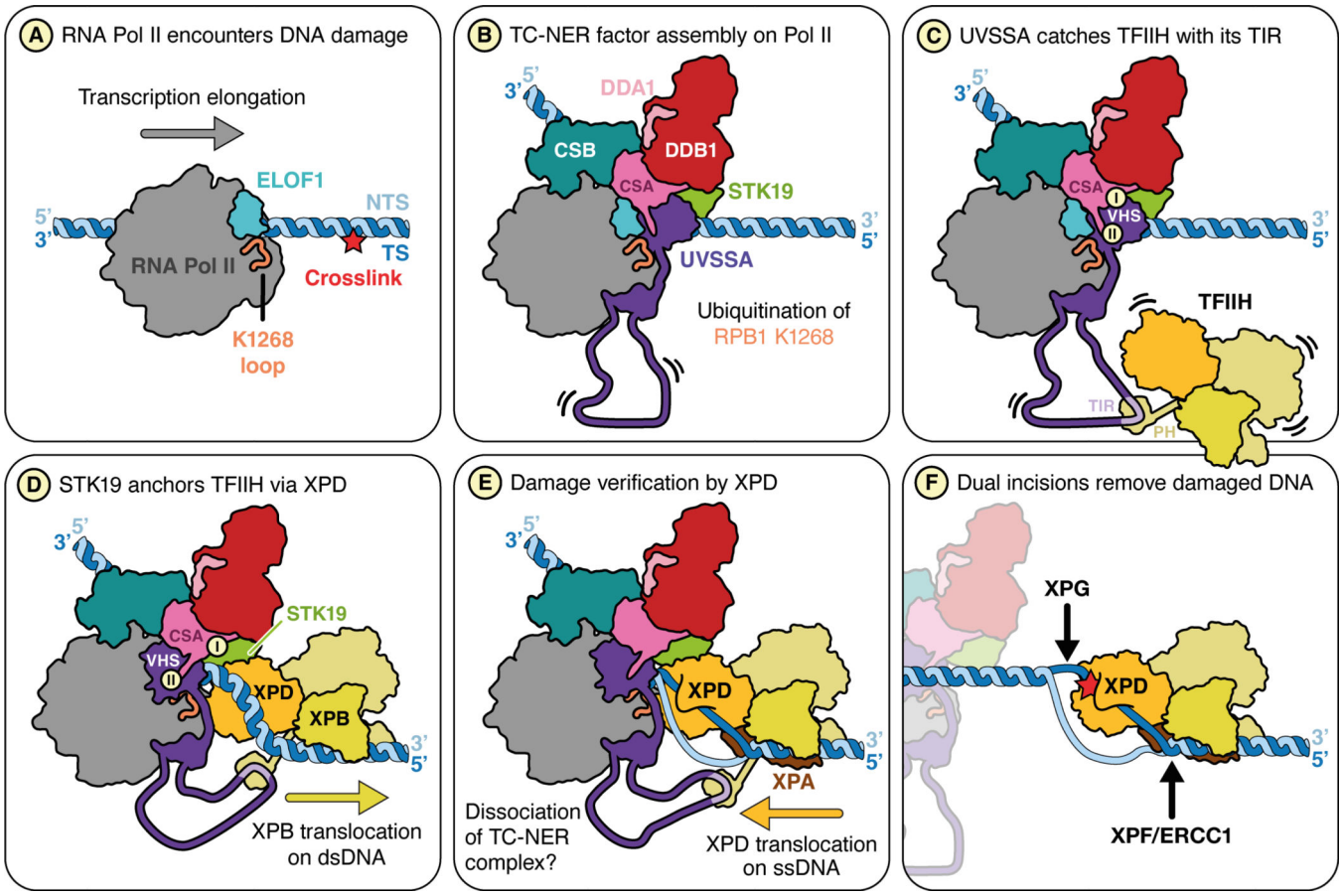

Figure 7. Model of STK19 function in TC-NER

(A) Pol II stalls at a lesion (red star) in the template strand (TS). NTS, non-template strand.

(B) TC-NER factors (CSB, $CRL4^{CSA}$ (CUL4A and RBX1 not depicted), UVSSA, ELOF1, and STK19) are assembled on stalled Pol II. Lysine residue 1268 of RPB1 (part of orange loop) is ubiquitinated by $CRL4^{CSA}$, which docks onto ELOF1 (ubiquitin not shown).

(C) The TFIIH-interacting region (TIR) of UVSSA binds to the p62 subunit of TFIIH, tethering TFIIH to the TC-NER complex. Since the TIR is located within a long, unstructured region of UVSSA (shown as a long loop), TFIIH can access a large area around the TC-NER complex. In this state, the N-terminal VHS domain of UVSSA interacts with the CSA β-propeller (I) as well as CSA's C-terminal tail (II).

(D) TFIIH is positioned by STK19 close to the downstream DNA. The VHS domain of UVSSA dissociates from the CSA β-propeller (I) but remains associated with CSA's C-terminus (II), allowing XPD to bind STK19. Due to STK19's interaction with XPD, TFIIH and therefore XPB are anchored relative to the damaged DNA. As a result, XPB translocation away from the TC-NER complex pumps DNA into the space between XPB and STK19, leading to DNA unwinding and template strand association with the XPD helicase channel.

(E) XPD translocates along the template strand in the 5'–3' direction to verify the damage. It is unclear whether the TC-NER complex is pushed back by TFIIH or whether it dissociates from DNA. This intermediate most closely resembles the structure modeled in Figure 5F.

(F) The structure-specific endonucleases XPF-ERCC1 and XPG perform dual incisions to remove the damaged DNA. Subsequent gap filling (not depicted) completes repair.

KEY RESOURCES TABLE

REAGENT or RESOURCE	SOURCE	IDENTIFIER
Antibodies		
Rabbit polyclonal anti-XPC CT Antigen: *X. laevis* XPC 1049–1062	This study	N/A
Rabbit polyclonal anti-XPC NT Antigen: *X. laevis* XPC 1–20	This study	N/A
Rabbit polyclonal anti-CSB Antigen: *X. laevis* CSB 1357–1370	This study	N/A
Rabbit polyclonal anti-CSA Antigen: *X. laevis* CSA 380–399	van der Weegen et al.[15]	N/A
Rabbit polyclonal anti-UVSSA Antigen: *X. laevis* UVSSA 718–737	This study	N/A
Rabbit polyclonal anti-STK19 Antigen: *X. laevis* STK19 1–15 (C9S)	This study	N/A
Rabbit polyclonal anti-RPB1 Antigen: $C(YSPTSPS)_4$	This study	N/A
Rabbit polyclonal anti-XPD Antigen: *X. laevis* XPD 741–760	This study	N/A
Rabbit polyclonal anti-ELOF1 Antigen: *X. laevis* ELOF1 full-length	This study	N/A
Rat monoclonal anti-RPB1 phospho-Ser5 (clone 3E8)	Kind gift from Stephen Buratowski	RRID:AB_2687451
Rat monoclonal anti-RPB1 phospho-Ser2 (clone 3E10)	Kind gift from Stephen Buratowski	RRID: AB_2784639
Rabbit polyclonal anti-TDG	Slenn et al.[47]	N/A
Rabbit polyclonal anti-H3	Cell Signaling Technology	Cat# 9715; RRID:AB 331563
Rabbit polyclonal anti-p97	Heubes et al.[49]	N/A
Mouse Anti-Rabbit IgG (H+L), unconjugated	Jackson ImmunoResearch	Cat# 211–005-109; RRID:AB 2339147
Mouse Anti-Rabbit IgG (L), HRP-conjugated	Jackson ImmunoResearch	Cat# 211–032-171; RRID:AB 2339149
Rabbit Anti-Mouse IgG (H+L), HRP-conjugated	Jackson ImmunoResearch	Cat# 315–035-003; RRID:AB 2340061
Goat Anti-Rat IgG (H+L), HRP-conjugated	Thermo Fisher Scientific	Cat# 31470 RRID:AB 228356
Bacterial and virus strains		
E. coli Rosetta 2(DE3)pLacI	Sigma-Aldrich	Cat# 71404–3
E. coli OverExpress C41(DE3)	Sigma-Aldrich	Cat# CMC0017
E. coli DH5α	NEB	Cat# C2987H
E. coli DH10EMBacY	Geneva Biotech	N/A
E. coli BL21-CodonPlus (DE3)-RIL	Agilent	Cat# 230245
Biological samples		
Sus scrofa thymus	Pel-Freez	Cat# 59451
Chemicals, peptides, and recombinant proteins		
BamHI-HF	NEB	Cat# R3136M
SacI-HF	NEB	Cat# R3156L
BbsI-HF	NEB	Cat# R3539L
PmlI	NFR	Cat# R0532S

REAGENT or RESOURCE	SOURCE	IDENTIFIER
EcoRI-HF	NEB	Cat# R3101S
KpnI-HF	NEB	Cat# R3142S
XhoI	NEB	Cat# R0146S
AflII	NEB	Cat# R0520S
I-CeuI	NEB	Cat# R0699S
NEBuilder HiFi DNA Assembly Master Mix	NEB	Cat# E2621L
Q5 Hot Start High-Fidelity 2X Master Mix	NEB	Cat# M0494L
QIAprep Spin Miniprep Kit	Qiagen	Cat# 27106
QIAquick Gel Extraction Kit	Qiagen	Cat# 28706
AMPure XP Reagent	Beckman	Cat# A63881
RNAClean XP	Beckman	Cat# A63987
cis-Diammineplatinum(II) dichloride	Sigma-Aldrich	Cat# P4394
ATP	Sigma-Aldrich	Cat# A5394
Phosphocreatine	Sigma-Aldrich	Cat# P6502
Creatine Phosphokinase	Sigma-Aldrich	Cat# C3755
DTT	Bio-Rad	Cat# 1610611
Nocodazole	Sigma-Aldrich	Cat# M1404
α-amanitin	Santa Cruz	Cat# sc-202440
Recombinant RNasin Ribonuclease Inhibitor	Promega	Cat# N2511
MLN4924	Active Biochem	Cat# A-1139
Proteinase K	Roche	Cat# 3115879001
[α-^{32}P]UTP	Revvity	Cat# BLU507H250UC
[α-^{32}P]dCTP	Revvity	Cat# BLU013H500UC
30% w/v Polyethylene glycol 20,000	Hampton Research	Cat# HR2–609
Xylene Cyanol FF	Sigma-Aldrich	Cat# X4126
Bromophenol Blue	Sigma-Aldrich	Cat# B0126
RNase A	Sigma-Aldrich	Cat# R5503
SYBR Gold Nucleic Acid Gel Stain	Invitrogen	Cat# S11494
Precision Plus Protein Dual Xtra Prestained Protein Standards	Bio-Rad	Cat# 1610377
AminoLink Coupling Resin	Thermo Fisher Scientific	Cat# 20382
rProtein A Sepharose Fast Flow	Cytiva	Cat# 17127903
Dynabeads Protein A	Invitrogen	Cat# 10001D
Protein A Mag Sepharose Xtra	Cytiva	Cat# 28967062
BSA	Fisher Scientific	Cat# BP1600–100
InstantBlue Protein Stain	Novus	Cat# ISB1L
One-Step Blue Protein Gel Stain	Biotium	Cat# 21003
SuperSignal West Dura Extended Duration Substrate	Thermo Fisher Scientific	Cat# 34075
complete EDTA-free Protease Inhibitor Cocktail	Roche	Cat# 11873580001
ANTI-FLAG M2 Affinity Gel	Sigma-Aldrich	Cat# A2220

REAGENT or RESOURCE	SOURCE	IDENTIFIER
3x FLAG Peptide	Sigma-Aldrich	Cat# F4799
Glutathione Sepharose 4B	Cytiva	Cat# GE17–0756-01
Ni-NTA Superflow resin	Qiagen	Cat# 30430
IPTG	Sigma-Aldrich	Cat# I5502
Lysozyme from chicken egg white	Sigma-Aldrich	Cat# L6876
Ubiquitin Activating Enzyme (E1)	R&D Systems	Cat# E-305–025
UBE2D2 (from E2 Screening Kit)	UBPBio	Cat# J1100
UBE2E1 (from E2 Screening Kit)	UBPBio	Cat# J1100
Recombinant Human Ubiquitin Protein, CF	R&D Systems	Cat# U-100H
ESF 921 Insect Ceii Cuiture Medium	Expression Systems	Cat# 96–001-01
Amyiose resin	NEB	Cat# E8021L
Leupeptin	RPI	Cat# L22035–0.050
Pepstatin A	AdipoGen	Cat# AGCP37001M100
PMSF	RPI	Cat# P20270–25.0
Benzamidine	RPI	Cat# B12000–100.0
Adenosine 5’-diphosphate sodium sait	Sigma-Aidrich	Cat# A2754
Beryiiium suifate tetrahydrate	Sigma-Aidrich	Cat# 202789
Sodium fiuoride	Sigma-Aidrich	Cat# 201154
Giutaraidehyde	EMS	Cat# 16200
Criticai commerciai assays		
TnT SP6 High-Yield Wheat Germ Protein Expression System	Promega	Cat# L3260
NEDD8 Conjugation Initiation Kit	R&D Systems	Cat# K-800
Deposited data		
Pol II TC-NER complex	This study	PDB: 9BZ0
Map i (Poi II TC-NER complex)	This study	EMDB: EMD-45050
Map ii (TC-NER factors)	This study	EMDB: EMD-47263
Map iii (CSB)	This study	EMDB: EMD-47262
Map iv (STK19)	This study	EMDB: EMD-47261
Map v (DDB1-DDA1)	This study	EMDB: EMD-47266
Map vi (UVSSA-DDB1-CSA)	This study	EMDB: EMD-47267
Map vii (RPB4/7)	This study	EMDB: EMD-47271
Map viii (DDA1)	This study	EMDB: EMD-47272
Map ix (Composite map)	This study	EMDB: EMD-47273
Experimental models: Cell lines		
Sf21 cells	Expression Systems	Cat# 94–003S
Sf9 cells	Expression Systems	Cat# 94–001S
Tni (Hi5) cells	Expression Systems	Cat# 94–002S
Experimental models: Organisms/strains		
Xenopus laevis (females)	Nasco	Cat# LM0053MX

REAGENT or RESOURCE	SOURCE	IDENTIFIER
Xenopus laevis (males)	Nasco	Cat# LM00715MX
Oligonucleotides		
See Table S2 for oligonucleotides and gene blocks	-	N/A
Recombinant DNA		
pTM07_5xUAS_AdML$^{\Delta 53}$_BbsI (referred to as pAdML$^{\Delta 53}$)	This study	N/A
pTM171_5xUAS_SCP2*_Ub_BbsI (referred to as pSCP2*)	This study	N/A
pTM180_5xUAS_SCP2*_Ub_BbsI_poiyA (referred to as pCtri-322)	This study	N/A
pTM181_5xUAS_SCP2*_BbsI_poiyA (referred to as pCtri-122)	This study	N/A
pTM210_5xUAS_SCP2*_Inverted-BbsI_poiyA (referred to as pCtri-NTS)	This study	N/A
pCMV-GFP (referred to as pCMV)	Matsuda & Cepko[50]	Addgene Cat# 11153
pActin	Barrows et al.[34]	N/A
pOPINK	Gift from Ray Owens	Addgene Cat# 41143
pOPINB	Gift from Ray Owens	Addgene Cat# 41142
pRJR1_GAL4-VP64	Stephen Buratowski	N/A
pET_hsTBP	Stephen Buratowski	N/A
pTM142_pAB1_FLAG-hsCSB^{WT}	van der Weegen et al.[15]	N/A
pTM143_pAB1_FLAG-hsCSB$^{\Delta CIM}$	van der Weegen et al.[15]	N/A
pTM449 pAB1_His6-TEV-Avi-xlDDB1_xlCSA^{WT}	This study	N/A
pTM451 pAB1 His6-TEV-Avi-xlDDB1_xlCSA^{Y-A}	This study	N/A
pTM450 pAB1 His6-TEV-Avi-xlDDB1_xlCSA^{WS-AA}	This study	N/A
pTM67_pAB1_FLAG-xlCUL4A_xlRBX1	van der Weegen et al.[15]	N/A
pTM185_pOPINK_xlELOF1^{WT}	van der Weegen et al.[17]	N/A
pTM194_pOPINK_xlELOF1^{SD-KK}	This study	N/A
pTM288_pOPINK_xlELOF1$^{NHE-AAA}$	This study	N/A
pTM81_pAB1_FLAG-xlUVSSA^{WT}	This study	N/A
pTM186_pOPINK_xlSTK19^{WT}	This study	N/A
pTM366_pOPINB_xlSTK19^{WT}	This study	N/A
pTM376_pOPINB_xlSTK19$^{\Delta N}$	This study	N/A
pTM367_pOPINB_xlSTK19^{4A}	This study	N/A
pTM378_pOPINB_xlSTK19$^{\Delta N\ 4A}$	This study	N/A
pTM377_pOPINB_xlSTK19^{DR-RD}	This study	N/A
pTM373_pOPINB_xlSTK19^{RY-GG}	This study	N/A
pTM374_pOPINB_xlSTK19^{D-R}	This study	N/A
pTM384_pOPINB_xlSTK19^{AS-EY}	This study	N/A
pTM506_pOPINB_xlSTK19$^{RYDAS-GGREY}$	This study	N/A
pTM408_pOPINB_xlSTK19^{R206A}	This study	N/A

REAGENT or RESOURCE	SOURCE	IDENTIFIER
pTM409_pOPINB_xlSTK19^{R207A}	This study	N/A
pTM399_pOPINB_xlSTK19$^{RR–AA}$	This study	N/A
pTM380_pOPINB_xlSTK19$^{RR–EE}$	This study	N/A
pTM365_pOPINB_hsSTK19^{WT}	This study	N/A
pF3A	Promega	Cat# L5671
pTM240_pF3A_xlUVSSA	This study	N/A
pTM242_pF3A_xlUVSSA$^{\Delta CIR}$	This study	N/A
pTM248_pF3A_xlUVSSA$^{\Delta TIR}$	This study	N/A
pTM252_pF3A_xlUVSSA$^{FV–AA}$	This study	N/A
pTM266_pF3A_xlUVSSA^{E10A}	This study	N/A
438-A	Gradia et al.[51]	Addgene Cat# 55218
438-B	Gradia et al.[51]	Addgene Cat# 55219
438-C	Gradia et al.[51]	Addgene Cat# 55220
1-B	Gradia et al.[51]	Addgene Cat# 29653
1-C	Gradia et al.[51]	Addgene Cat# 29654
438-C_NHis6-TEV-CSB$^{V1097M, G1213R, R1413Q}$	This study	N/A
438-B_NHis6-TEV-DDB1+ERCC8	This study	N/A
438-B_NHis6-TEV-UVSSA	This study	N/A
1-B NHis6-TEV-ELOF1	This study	N/A
1-C_NHis6-MBP-N10-TEV-DDA1	This study	N/A
Software and algorithms		
ImageJ2 - Fiji (version 2.14)	Schindelin et ai.[52]	https://imagej.net/software/fiji/
GraphPad Prism (version 10.2.2)	GraphPad Software Inc.	https://www.graphpad.com/
Octet Anaiysis Studio (version 13.0)	Sartorius	N/A
cryoSPARC (version 4.4.1)	Punjani et ai.[53]	https://www.cryosparc.com
PHENIX (version 1.20.1)	Liebschner et ai.[54]	https://phenix-oniine.org/
ISOLDE (version 1.7.1)	Croii[55]	https://tristanic.github.io/isolde/
UCSF ChimeraX (versions 1.6–1.7)	Goddard et ai.[56]	https://www.cgi.ucsf.edu/chimerax/
Adobe Iiiustrator (version 28.7.1)	Adobe	https://www.adobe.com/products/iiiustrator.html
Other		
HiLoad 16/600 Superdex 75 pg column	Cytiva	Cat# 28989333
HiLoad 16/600 Superdex 200 pg column	Cytiva	Cat# 28989335
Superdex 200 Increase 10/300 GL column	Cytiva	Cat# 28990944
Superose 6 Increase 10/300 GL column	Cytiva	Cat# 29091596
Superose 6 Increase 3.2/300	Cytiva	Cat# 29091598
Mono Q 5/50 GL column	Cytiva	Cat# 17516601
GSTrap HP column	Cytiva	Cat# 17528202
HisTrap HP column	Cytiva	Cat# 17524802

REAGENT or RESOURCE	SOURCE	IDENTIFIER
HiTrap Q HP column	Cytiva	Cat# 17115301
HiTrap Heparin HP column	Cytiva	Cat# 17040701
HiTrap SP HP column	Cytiva	Cat# 17115101
XK column 16/20 column	Cytiva	Cat# 28988937
Typhoon FLA 7000 phosphorimager	GE Heaithcare	N/A
Typhoon 5	GE Heaithcare	N/A
Amersham Imager 600	GE Heaithcare	N/A
4–15% Mini-PROTEAN TGX Precast Protein Gels	Bio-Rad	Cat# 4561086
4–15% Criterion TGX Precast Midi Protein Gels	Bio-Rad	Cat# 5671085
7.5% Mini-PROTEAN TGX Precast Protein Gels	Bio-Rad	Cat# 4561026
NuPAGE 4–12% Bis-Tris protein gels	Invitrogen	Cat# NP0321BOX
PVDF membranes	VWR	Cat# PI88518
Octet RED384 system	Sartorius	N/A
Octet Streptavidin (SA) Biosensor	Sartorius	Cat# 18–5019
Octet 384 Well Tilted Bottom Plates	Sartorius	Cat# 18–5080
UltrAuFoil R 2/2 (200 Mesh)	Quantifoii	Cat# N1-A16nAu20–01
Vitrobot Mark IV	FEI/Thermo Fisher Scientific	N/A
Titan Krios + Falcon 4i + Selectris Energy Filter	FEI/Thermo Fisher Scientific	N/A